8-9-2017 12:00 AM

Simulation of driven elastic spheres in a Newtonian fluid

Shikhar M. Dwivedi, *The University of Western ontario*

Supervisor: Dr. Colin Denniston, *The University of Western Ontario*

A thesis submitted in partial fulfillment of the requirements for the Master of Science degree in Applied Mathematics

Recommended Citation

Abstract

Simulations help us test various restrictions/assumptions placed on physical systems that would otherwise be difficult to efficiently explore experimentally. For example, the Scallop Theorem, first stated in 1977, places limitations on the propulsion mechanisms available to microscopic objects in fluids. In particular, the theorem states that when the viscous forces in a fluid dominate the inertial forces associated with a physical body, such a physical body cannot generate propulsion by means of reciprocal motion. The focus of this thesis is to firstly, explore an adaptive multiple-timestep (MTS) scheme for faster molecular dynamics simulations (MD), and secondly to use hybrid MD-LBM (Lattice-Boltzman Method) to test the Scallop Theorem's restrictions using an elastic spherical swimmer. The work begins with developing and demonstrating an adaptive MTS technique that reduces the run time of single timestep (STS) velocity-Verlet integration scheme. Later we discuss our simulation, which uses the MD-LBM to simulate a elastic spherical swimmer in a water-like fluid and prove that the swimmer indeed overcomes the Scallop Theorem. We investigate the relation between the swimmer's physical behaviour (speed, frequency) and its properties (radius, bulk modulus etc).

Keywords: elastic swimmers, overcoming Scallop theorem, inertial swimmers, velocity-Verlet, adaptive velocity-Verlet

Co-Authorship Statement

The work for chapter 2 and chapter 3 was done in collaboration with my supervisor Dr. Colin Denniston. The work described in chapter 2 is in progress and is being developed into an article for publication. Chapter 3 has been submitted as a regular article to Physical Review Fluids. Chapter 3 has three authors. The project was started by David Urbanik (summer student). I extended the work and analysis, and all simulations shown here were performed by myself. Dr. Denniston actively participated in and guided the research. Dr. Denniston also helped me write the paper (article).

Contents

List of Figures

Chapter 1

Introduction

Most living organisms, including humans, are highly dependent on the motility of micro-sized cellular swimmers. Natural biological micro-swimmers, often just referred to as *swimmers*, were an important step in evolution. The ability of micro-organisms to swim towards a food/energy source meant that they could thrive easily. An important example are sperm cells which swim using flagella (very effectively, even against currents [9]) and transport the male DNA to eggs in various species. Other microbes such as bacteria and algae are efficient swimmers too. These cells and microbes perform functions that are highly specific and choose their preferred direction of swimming (towards or away) based on many factors such as light (photoaxis), chemical stimulus (chemotaxis), gravity (gravitaxis) and shear regions (gyrotaxis).

Since swimmers play such an important role in the biological domain, from performing normal day-to-day functions inside our bodies to spreading deadly diseases, it is very important for us to understand their behavior. A good point to start is to ask the question - *"How do these biological swimmers swim?"*.

Researchers have indeed been focused on replicating the behavior of natural swimmers to better understand how they swim [1] [20]. Such efforts have been, for the most part, the beginning of the research in the field of micro-swimmers. Only recently, over a decade ago, did the focus move to artificial swimmers, when researchers realized artificial swimmers are not constrained by many of the physical factors which govern the behavior of living cells (such

as elastic properties of organic material, etc.) and can be driven much faster [7].

Manufacturing microscopic objects often cannot be achieved by just scaling down the "conventional machinery". Extremely small length scales put severe restrictions on operation, design, and usable materials for constructing such objects. Hence, novel approaches in the design of artificial swimmers are needed. With advances in materials science, now there is a lot more choice in terms of material (not bound to just organic matter) to construct such swimmers and means to actuate them (external magnetic fields, electric fields, etc). This makes it possible to design swimmers that are not necessarily bio-inspired. Applications of such swimmers include, but are not limited to, transportation of cargo (such as drugs) to a targeted location, microfluidics, and catalyzing reactions [17] [32] [16] [36] [3]. Various approaches have been taken to achieve propulsion by such a swimmer in a fluid. Broadly, the two common approaches are: building a hybrid (an artificially modified natural micro-organism/cell) and completely artificial swimmers.

The design of an artificial micro-swimmer is a challenging task, both scientifically and from the engineering perspective. In our research we are more concerned with the scientific aspects as it paves the way for the latter. On microscopic scales in fluids the Reynolds number, which is the ratio of inertial forces to the viscous forces in a fluid, is low (¡¡1) and viscous forces dominate inertial forces. When we swim, our propulsion forward in fluid (water, unless one is a daring swimmer who prefers more exotic fluids), is mostly because of inertia given our macroscopic sizes compared to the fluid particles. But for a micro-swimmer to swim in water is equivalent to a human swimming in a gel. The effect is described by the *Scallop Theorem* [22]. Before we proceed further, it is important to state and explain the Scallop Theorem.

1.1   Scallop Theorem

E.M. Purcell, in 1977, stated in a paper titled "Life at low Reynolds number", what has now come to be known as the Scallop Theorem [22]. In essence, it simply states that, *"an object in a Newtonian fluid at low Reynolds number cannot achieve propulsion through reciprocal*
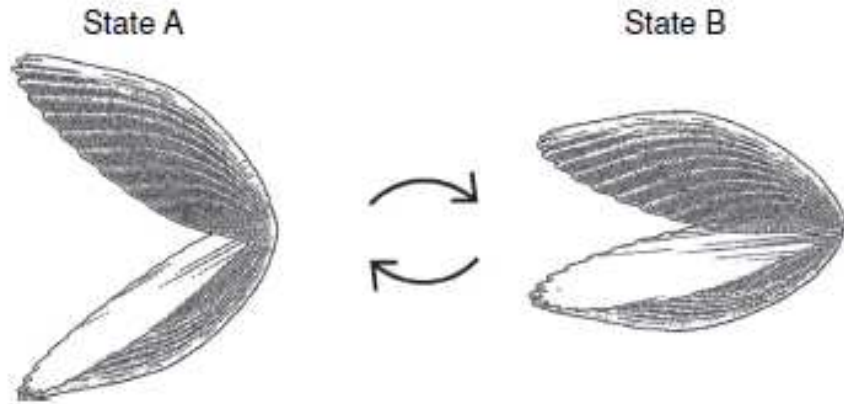
Figure 1.1: A scallop moving reciprocally and retracing its trajectory [23].

motion". This means that if an object goes through time-reversible periodic motion it cannot move forward. For example, consider a scallop, it opens its shell slowly and closes it fast. A scallop only has one hinge and hence only one degree of freedom in configuration space and hence bound to make reciprocal motion. What ends up happening in this case is the scallop would move from state A to B and retrace its trajectory in an endless fashion without ever getting anywhere, as show in figure 1.1 [23].

It is worth noting that G.I. Taylor had already demonstrated similar constraints on the reciprocal swimmers in low Reynolds number fluids via experiments using physically constructed swimmers [28]. E.M Purcell attended one of the Taylor's demonstrations and later expanded and popularized the work in the paper titled "Life at low Reynolds number".

Before we go further, let's take some time to explain a couple of strategies Purcell acknowledged can be exploited by a micro-being to be able to bypass the Scallop Theorem.

The first strategy is related to degrees of freedom. Purcell recognized and mentioned in his paper that the hopelessness the Scallop Theorem brought upon a micro-swimmer is only absolute for a being who has only one degree of freedom. For if a being has more, say two degrees of freedom, they can devise novel ways to move in a non-reciprocal fashion. One such example is shown in figure 1.2 (redrawn, based on [22]).

A second way to get around the Scallop Theorem, is the flexible oar strategy. If such an
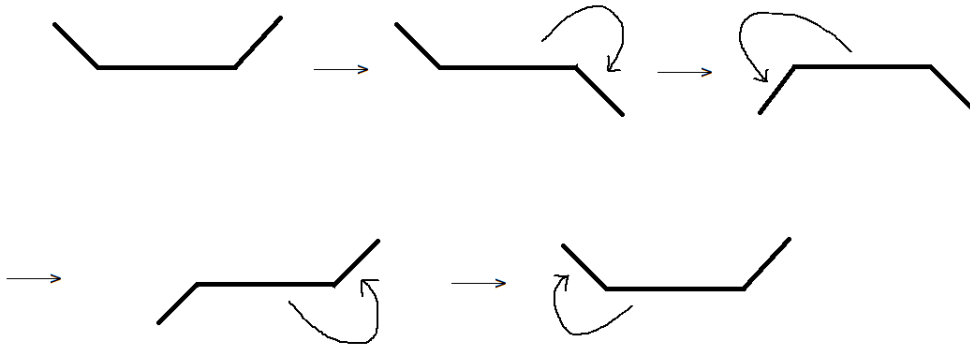
Figure 1.2: A micro-swimmer with two degrees of freedom exhibiting a non-time-reversible movement (redrawn based on [22]).

object has a flexible oar it can bend the object one-way and then the other, propelling itself forward. Some models essentially use the flexible oar strategy to propel themselves forward [37].

To summarize the discussion about the Scallop Theorem, what actually needs to be done to propel a micro-swimmer is one of these things: somehow make inertia important in a fluid at the length scales where it is not dominant; or exploit multiple degrees of freedom to move non-reciprocally. Among the two options mentioned above, the first option inertia, has largely been ignored. Driving a swimmer at microscopic length scales is usually assumed to make inertia negligible compared to viscous forces. Multiple degrees of freedom, however, has been the primary tool to overcome the Scallop theorem and has been used to drive swimmers. Many model swimmers use bead and spring models, which have multiple degrees of freedom, and exploit them to propel themselves in the fluid.

But, that is the story in Newtonian fluids. A curious reader might ask, aren't most of the biological fluids (where most of the swimmers live naturally), non-Newtonian and complex fluids? Wouldn't the elasticity of such fluids affect the swimmer? And the answer is yes. Research has shown that in such non-Newtonian fluids, reciprocal motion can indeed propel the swimmer [23]. In non-Newtonian fluids even a reciprocal motion can generate propulsion

as the fluid itself is visco-elastic.

1.2 Inertia and its importance in micro-swimmers

1.2.1 Rigid bodies

As explained earlier, at low Reynolds number, inertia is assumed to be a negligible source of propulsion for micro-swimmers. But there are effects of inertia on a neutrally buoyant rigid sphere in a moving fluid that have been known since 1962. G. Segre and A. Silberberg in their papers titled "Behaviour of macroscopic rigid spheres in Poiseuille's flow part 1" [24] and "Behaviour of macroscopic rigid spheres in Poiseuille's flow part 2" [25], show that when spheres of sub-millimeter size radii are put inside a vertical tube (of radius on the order of a few mm) with Poiseuille flow, they tend to choose a equilibrium path along the flow which is not at the center of the tube, suggesting there is a sideways force acting on them. This was a deviation from previous predictions [26], which did not account for the inertia terms of the equations of motion *or* the presence of the rigid walls, and suggested no radial movement of a rigid sphere carried should occur in an unbounded Poiseuille flow. It was demonstrated by Serge *et al.* that such a radial force is due to the effects of the time derivative terms in the Navier-Stokes equations, which are inertial terms.

A pictorial depiction of this phenomenon is shown in figure 3.8 (redrawn, based on [19]). The arrows to the left of the figure represent the fluid velocity (longer arrow length implies higher velocity) in a cylindrical Poiseuille flow. The flow is bounded by walls perpendicular to its direction of flow. It can be seen how the wall effect and shear forces eventually bring the spheres from their random initial positions (at t=0) along the flow to a equilibrium position on a preferred channel along the direction of flow (at t=T). This migration is the result of inertial forces and is called the *tubular pinch effect*. The equilibrium position at which the particle settles itself in the flow depends on the particle's radius and the flow (tube) width.

The reason why inertia comes in to play at a length scale where the Reynolds number is minuscule, can be explained in many ways. One way is to consider the Reynolds number , Re,
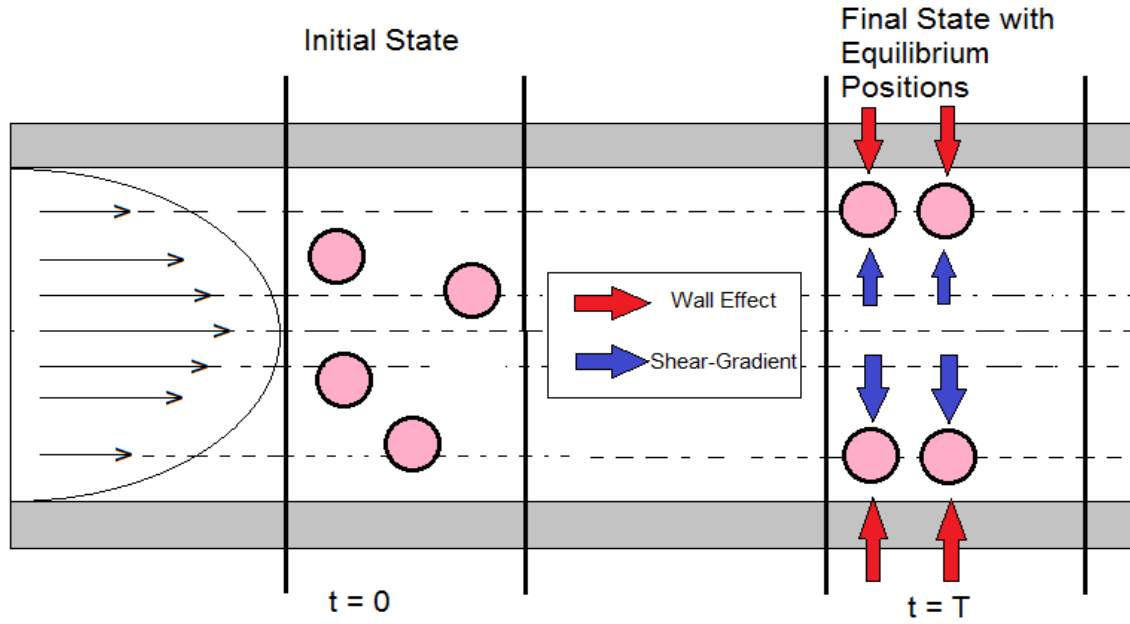
Figure 1.3:   Neutrally buoyant rigid spheres *settling* in their equilibrium paths along the direction of Poiseuille flow (redrawn, based on [19]). The equilibrium position of each particle depends on its radius and the flow (tube) width.

definition :

$$Re = \frac{\rho v L}{\eta},\tag{1.1}$$

where ρ is the density of the fluid, v is the velocity of the fluid, L is the characteristic length and η is the shear viscosity.

It is clear from the equation that at microscopic lengths the Reynolds number would be very small, which would, in turn, suggest that the viscous force should dominate. But there is an important aspect to note here: the characteristic length L would normally be assumed to be of the order of the particle diameter (in the case of spherical particles) but it is not. For example, let's consider a case where a particle is allowed to be in the flow for long periods of time, allowing it to travel long distances compared to its characteristic size L. In such circumstances, the effective characteristic length L^* changes to the larger value, the distance traveled. This increases the effective Reynolds number and hence makes inertial terms in Navier-Stokes

equation non-zero.

1.2.2 Flexible bodies

In our group's research (described in chapter 3), the swimmer is an elastic spherical swimmer. The previous discussion although valid for rigid particles in a bounded flow, does not account for the effects observed in more complicated cases such as our simulation, which uses a flexible spherical swimmer. To the best of our knowledge, no one has demonstrated a sizable contribution of inertia to the propulsion of a neutrally buoyant micro-swimmer in a Newtonian fluid. Swimmers in unbounded medium (such as our simulation, which is unbounded in two dimensions and bounded in one) can travel far and hence, its not clear that we can safely ignore their inertia altogether. This prompted us to investigate the extent of the contribution of inertia to our swimmer's propulsion, which is discussed in detail in chapter 3. To summarize, we found that the elastic media of the spherical sphere (which has several degrees of freedom), allows the storage of inertia which results in non-reciprocal motion when driven in a Newtonian fluid. The sphere uses this inertia to advance itself once it breaks the symmetry and starts to propel itself in a chosen direction.

1.3 Methodologies

A few of the most common methods for simulations used today are Molecular Dynamics and Monte Carlo methods for particles, and Lattice-Boltzmann method (LBM) for fluids. There is also hybrid MD-LBM, when particles are interacting with the LB fluid. We used LAMMPS (Large-Scale Atomistic/Molecular Massively Parallel Simulator), which is a simulation tool, for our simulations. We used a package within LAMMPS called lb_fluid that provides an implementation of the hybrid MD-LBM method due to Mackay et al. [15].

We also investigated MD simulations using velocity-Verlet. Velocity-Verlet is the default equation of motion integrator in LAMMPS. It provides a stable and accurate scheme for integration. The implementation of velocity-Verlet in LAMMPS is a single timestep (STS) scheme.

During a simulation, the accuracy of trajectories is restricted by the correct solution for the particles whose trajectories require solutions on the shortest time scale. This presents a bottleneck in terms of simulation speed as the entire system is restricted by the fastest (shortest time scale) phenomenon in the entire system. Hence, at any given time there could be a fraction of the system's particles that are under enough force (acceleration) to bring down the time scale of entire system significantly.

This prompted us to devise a technique to implement adaptive multiple time scale velocity-Verlet. Although such a scheme (non-adaptive) is already available in LAMMPS it is only applicable for certain potentials and needs to be configured manually depending on the potentials used. Present run time performance gains are restricted to about a factor of 4.

We explore various versions of velocity-Verlet schemes in detail in chapter two and show why an adaptive, multiple timestep velocity-Verlet could lead to significant speed up.

1.4   LAMMPS

Our simulation, presented in chapter three, was performed by using an open source tool called LAMMPS. It is hence worthwhile to give a brief overview of the tool. LAMMPS is an open source MD simulation tool. It comes with a scripting language that can be used to define the system and run simulations. A simulation in LAMMPS can be dynamically modified depending on a number of system characteristics. It has multiple implementations of every component that goes in to a MD simulation, hence a very wide range of systems can be simulated. The major components in a MD simulation and some of the corresponding choices available in LAMMPS are described below -

- Simulation Box - Cuboid, Spherical, etc.

- Boundary Condition - Fixed or periodic.

- Bonds - Harmonic, Covalent, etc.

- Potentials - Lennard Jones, Coulomb, etc.

Various commands for modifying the system, measuring the system properties, re-starting simulation, etc, are also available. LAMMPS has been successfully used by researchers for fluid dynamics, solid state and bio-polymer simulations etc.

Please see LAMMPS documentation available online for more details [11].

1.5   Summary of subsequent chapters

In chapter two, we examine MD methodologies used for simulations. In particular, we focus on a popular numerical integration scheme called velocity-Verlet. We begin by implementing a commonly used non-adaptive version of velocity-Verlet, and then implement an adaptive single timestep version. We demonstrate that the adaptive version leads to better performance. We also discuss the controls (both active and passive) that can be used to select timestep values and *control* such an adaptive simulation. Finally, we introduce a multiple timestep (MTS) version of the scheme. We demonstrate why and how this scheme is substantially better than the non-adaptive and adaptive single timestep schemes, and that it leads to significant performance gains.

In chapter three, we discuss the simulation of a driven elastic sphere in a Newtonian fluid using LAMMPS. We begin with discussing the construction of the elastic sphere and the model used for the driving scheme, and present results including the velocities achieved by the sphere using several different simulation parameters. Various other aspects of the results obtained are then analyzed, including the variation of the velocities attained by varying the sphere diameter, sphere stiffness and driving amplitude. The contribution of inertia to the sphere's driving is then investigated. We conclude the chapter by comparing our results with available similar, but not exact, theoretical predictions [6] and summarizing the chapter.

In chapter 4, we summarize the thesis and present conclusions and possible applications of our research.

Chapter 2

Multiple Timestep (MTS) Adaptive velocity-Verlet Scheme

2.1   Introduction

When solving Newton's equations of motion accuracy and conservation of thermodynamic quantities, such as total energy of the system are of importance. An accurate scheme characterized by small truncation errors is not always symplectic, often resulting in poor energy conservation. This is why velocity-Verlet [33] is a very commonly used scheme in MD simulations. Apart from being symplectic, it is also fairly accurate. In our research which uses LAMMPS, the default integrator used is velocity-Verlet. It hence made sense to investigate the properties of the scheme, and analyze its strengths and weaknesses.

For a scheme that's been used as extensively as velocity-Verlet, a quality in-depth discussion and analysis of the scheme is very scarce. In this chapter we derive the scheme from scratch and later use it to test Newtonian systems with non-bonded pairwise interactions using the Lennard-Jones potential and investigate merits of using the adaptive, multiple timestep scheme versus the single timestep schemes (both non-adaptive and adaptive).

10

2.2 velocity-Verlet Scheme

2.2.1 Derivation

Velocity-Verlet [33] is a form of the Verlet scheme, where the position is calculated depending only on the position during the last timestep instead of positions during the last two timesteps. Starting with the expression for position given by $x(t + h)$, where t is the time and h is a small timestep, and taking Taylor's expansion for position:

$$x(t + h) \approx x(t) + hv(t) + \frac{h^2}{2!}a(t) + \left[\frac{h^3}{3!}\dddot{x}(t) + \frac{h^4}{4!}\ddddot{x}(t)\right].$$ (2.1)

We will be tracking two truncation error terms and they will be kept in square brackets, as shown in equation (2.1).

In equation (2.1), we can get the acceleration term a(t) from the potential using Newton's equation of motion F = ma. The velocity value at $t + h$, using Taylor's expansion again is:

$$v(t + h) \approx v(t) + ha(t) + \frac{h^2}{2!}\dot{a}(t) + \left[\frac{h^3}{3!}\dddot{v}(t) + \frac{h^4}{4!}\ddddot{v}(t)\right].$$ (2.2)

We do not have value of $\dot{a}(t)$, so lets derive it. Expanding $a(t + h)$ through Taylor's series expansion:

$$a(t + h) \approx a(t) + h\dot{a}(t) + \left[\frac{h^2}{2!}\ddot{a}(t) + \frac{h^3}{3!}\dddot{a}(t)\right],$$ (2.3)

or

$$a(t + h) \approx a(t) + h\dot{a}(t) + \left[\frac{h^2}{2!}\dddot{v}(t) + \frac{h^3}{3!}\ddddot{v}(t)\right].$$ (2.4)

Rearranging this equation:

$$\dot{a}(t) \approx \frac{a(t + h) - a(t)}{h} - \left[\frac{h}{2!}\dddot{v}(t) + \frac{h^2}{3!}\ddddot{v}(t)\right].$$ (2.5)

Using the value of $\dot{a}(t)$ from equation (2.5) in equation (2.2) , we get:

$$v(t + h) \approx v(t) + h\frac{a(t + h) + a(t)}{2} + \left[\dddot{v}(t)\left(\frac{h^3}{6} - \frac{h^3}{4}\right) + \ddddot{v}(t)\left(\frac{h^4}{24} - \frac{h^4}{12}\right)\right], \qquad (2.6)$$

or rewriting derivatives of v in terms of derivatives of x:

$$v(t + h) \approx v(t) + h\frac{a(t + h) + a(t)}{2} + \left[\ddddot{x}(t)\left(\frac{h^3}{6} - \frac{h^3}{4}\right) + \overset{(5)}{x}(t)\left(\frac{h^4}{24} - \frac{h^4}{12}\right)\right]. \qquad (2.7)$$

Simplifying ,

$$v(t + h) = v(t) + h\frac{a(t + h) + a(t)}{2} - \left[\ddddot{x}(t)\left(\frac{h^3}{12}\right) + \overset{(5)}{x}(t)\left(\frac{h^4}{24}\right)\right], \qquad (2.8)$$

and, hence we have the two most important equations of velocity-Verlet method - equation (2.1) for calculating position and equation (2.8) for calculating velocity.

In summary the velocity-Verlet Scheme works as follows:

(Please note that the truncation error terms(in big square brackets) are given here for later analysis. They are not used in the actual calculation.)

- **STEP 1.** Calculate position using equation (2.1):

$$x(t + h) \approx x(t) + hv(t) + \frac{h^2}{2!}a(t) + \left[\frac{h^3}{3!}\dddot{x}(t) + \frac{h^4}{4!}\ddddot{x}(t)\right]. \qquad (2.9)$$

- **STEP 2.** Calculate acceleration using Newton's second law of motion, $F = ma$:

$$a(t + h) = \frac{F(t + h)}{m}. \qquad (2.10)$$

$F(t + h)$ can be calculated by using the potential(s) acting on the particles, which are functions of $x(t + h)$, obtained in step 1.

- **STEP 3.** Calculate Velocity using equation (2.8):

$$v(t + h) \approx v(t) + h\frac{a(t + h) + a(t)}{2} - \left[\ddddot{x}(t)\left(\frac{h^3}{12}\right) + \overset{(5)}{x}(t)\left(\frac{h^4}{24}\right)\right]. \qquad (2.11)$$

Step 1-3 are repeated at each timestep, for each particle.

2.2.2   Derivation of truncation error in velocity-Verlet

The error in velocity-Verlet is of 4th order in position, and 3rd order in velocity. However, the 4th order error in position is not apparent from equation (2.9). Let's derive the error order for position.

Lets substitute $t \rightarrow t - h$ in equation (2.9):

$$x(t) \approx x(t-h) + hv(t-h) + \frac{h^2}{2!}a(t-h) + \left[\frac{h^3}{3!}\dddot{x}(t-h) + \frac{h^4}{4!}\ddddot{x}(t-h)\right]. \qquad (2.12)$$

Adding this equation to equation (2.9) we get:

$$x(t+h) + x(t-h) \approx 2x(t) + h\left(v(t) - v(t-h)\right) + \frac{h^2}{2}\left(a(t) - a(t-h)\right)$$
$$+ \frac{h^3}{3!}\left(\dddot{x}(t) - \dddot{x}(t-h)\right) + \frac{h^4}{4!}\left(\ddddot{x}(t) - \ddddot{x}(t-h)\right). \quad (2.13)$$

Now using equation (2.11) to simplify this, we get:

$$x(t+h) + x(t-h) \approx 2x(t) + h^2 a(t) - h\left[\dddot{x}(t-h)\left(\frac{h^3}{12}\right) + x(t \overset{(5)}{-} h)\left(\frac{h^4}{24}\right)\right]$$
$$+ \frac{h^4}{3!}\dddot{x}(t) + \frac{h^5}{4!}\overset{(5)}{x}(t). \quad (2.14)$$

Which is simplified to :

$$x(t+h) \approx 2x(t) - x(t-h) + h^2 a(t) + \left[\frac{h^4}{12}\ddddot{x}(t)\right]. \qquad (2.15)$$

Which is basically of the form of the basic Verlet and truncation error being:

$$\tau_e = \frac{h^4}{12}\ddddot{x}(t). \qquad (2.16)$$

Let's calculate an approximation of the truncation error. As the error τ_e is basically proportional to the second derivative of acceleration, using the Taylor's series expansion of $a(t+h)$ and $a(t-h)$, and adding them, we get:

$$\ddot{a}(t) \approx \frac{a(t+h) - 2a(t) + a(t-h)}{h^2} - \frac{h^2}{12}\overset{....}{a}(t). \tag{2.17}$$

Substituting the value of $\ddot{a}$ from this equation in eq. (2.16), we get the following steps:

$$\tau_e = \frac{h^4}{12}\overset{......}{x}(t), \tag{2.18}$$

$$\implies \tau_e = \frac{h^4}{12}\ddot{a}(t), \tag{2.19}$$

$$\implies \tau_e \approx \frac{h^4}{12}\left(\frac{a(t+h) - 2a(t) + a(t-h)}{h^2} - \frac{h^2}{12}\overset{....}{a}(t)\right), \tag{2.20}$$

$$\implies \tau_e \approx \frac{h^2}{12}\Big(a(t+h) - 2a(t) + a(t-h)\Big) - O(h^6), \tag{2.21}$$

or,

$$\implies \tau_e \approx \frac{h^2}{12}\Big(a(t+h) - 2a(t) + a(t-h)\Big). \tag{2.22}$$

We have used this expression for estimating truncation error in position for our analysis further in this chapter.

2.3   Stability of velocity-Verlet Scheme

Lets consider a simple system consisting of one particle moving under a harmonic force, given by:

$$F(x) = -kx. \tag{2.23}$$

Since, velocity-Verlet and Verlet both have the same properties in terms of calculating the position, let's consider the Verlet scheme for simplicity. The equation to calculate the position at any given time $t + h$ in the Verlet scheme is given by equation (2.15):

$$x(t + h) \approx 2x(t) - x(t - h) + h^2 a(t) + O(h^4). \tag{2.24}$$

Consider that this equation is being applied to a system consisting of one particle whose motion is described by equation (2.23). In such case the acceleration of the particle is given by:

$$a(t) = \frac{F(t)}{m}, \tag{2.25}$$

where $F(t)$, according to equation(2.23) is given by:

$$F(t) = -kx(t). \tag{2.26}$$

Combining equation (2.25) and equation (2.26), we get:

$$a(t) = \frac{-kx(t)}{m}. \tag{2.27}$$

Using this equation in equation (2.24), and dropping the error term, we get the following linear difference equation:

$$x(t + h) = 2x(t) - x(t - h) - kh^2 \frac{x(t)}{m}, \tag{2.28}$$

which is homogeneous. Without loss of generality, let us assume that the mass of the particle is equal to 1 or $m = 1$ for simplicity. This is equivalent to setting units of mass and we have used this value for mass for all the particles in all of our simulations. The characteristic equation for equation (2.28) is:

$$\lambda^2 + (kh^2 - 2)\lambda + 1 = 0. \tag{2.29}$$

The roots for equation (2.29) are given by:

$$\lambda = \frac{-(kh^2 - 2) \pm \sqrt{(kh^2 - 2)^2 - 4}}{2}. \tag{2.30}$$

The condition for stability of such a difference equation is that the characteristic roots (or absolute value of characteristic roots, in cases where the characteristic roots are imaginary) be less than 1.

Under such a constraint, solving for the stability criteria we get the following relation:

$$\left| \frac{-(kh^2 - 2) \pm \sqrt{(kh^2 - 2)^2 - 4}}{2} \right| < 1. \tag{2.31}$$

On solving, this results in:

$$h < \frac{2}{\sqrt{k}}. \tag{2.32}$$

Plugging eq. (2.32) into eq. (2.31), it is clear this value of h makes eq. (2.31) an equality.

2.3.1   Testing the stability criteria

Let us put the stability criteria given by equation (2.32), derived for the above mentioned system to test.

The solution to the equation of motion for such a particle with $k = 1$ is:

$$x(t) = A \cos(\omega t). \tag{2.33}$$

Let us assume the initial condition to be $x(0) = 10$, which makes $A = 10$. If we use the Verlet scheme to solve the equation of motion for such a particle, the stability criteria demands that the timestep h be constrained by:

$$h < 2. \tag{2.34}$$

The results for such a simulation, using both velocity-Verlet and Verlet scheme, with timesteps $h = 1.99$, $h = 2.005$ and $h = 0.007$ (a typically used value of timestep in MD simulations using velocity-Verlet) are shown in Fig. 2.1(a) and 2.1(b). Notice how a slightly higher value for h (2.005) than the stability criteria $h = 2$, results in inaccurate position values when integrated. The same results are observed for both Verlet and velocity-Verlet as both are
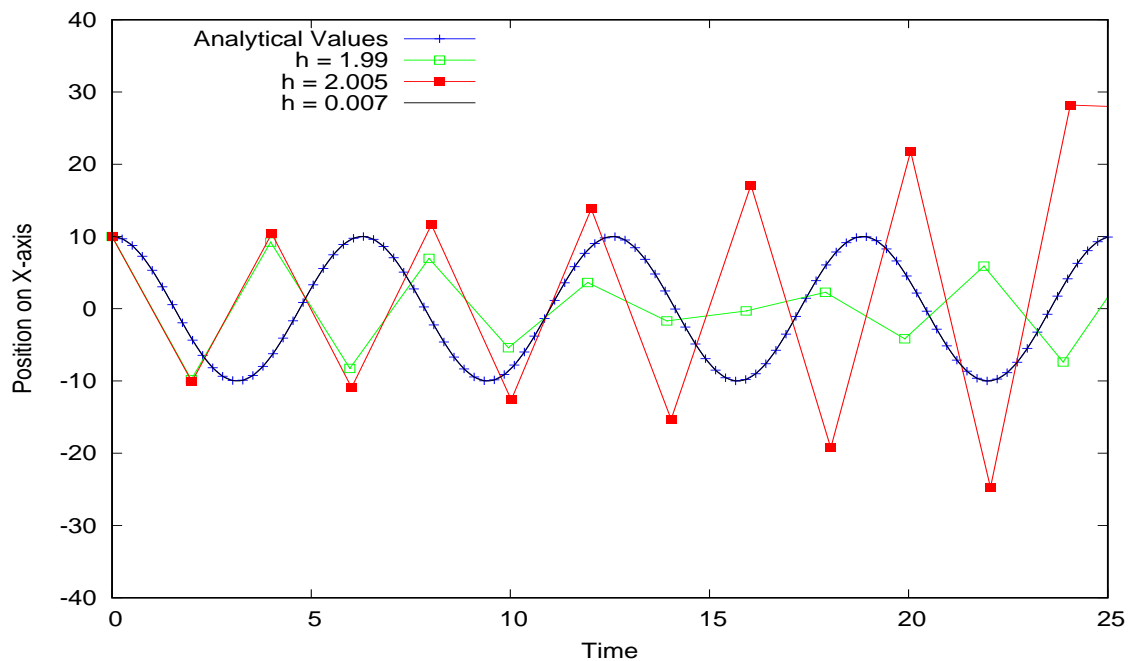
(a)
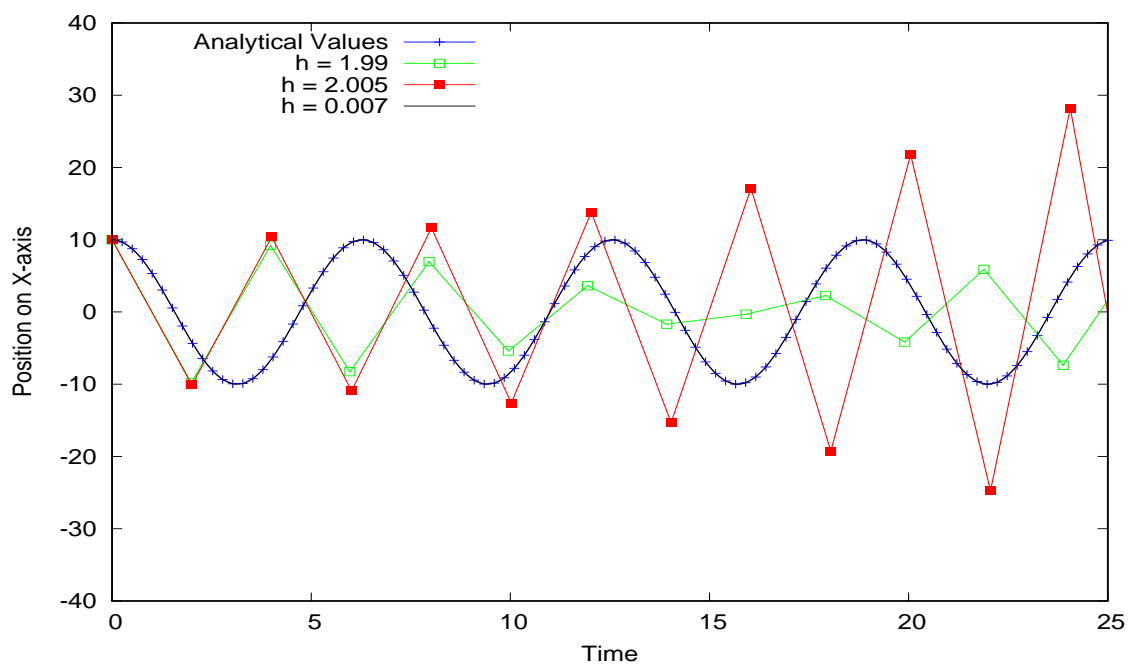
(b)

Figure 2.1: Comparison of the analytical solution for the position of a particle to the position calculated by the velocity-Verlet scheme (Fig. a), and the Verlet scheme (Fig. b), using timesteps slightly smaller (1.99) and slightly larger (2.005) than the stability criteria (2.0) and a typical MD timestep (0.007).

essentially identical schemes when it comes to calculating position. The figures also show the analytical solution and solution using $h = 0.007$. At the sufficiently lower h (0.007) compared to the stability criteria $h = 2$, the solution completely overlaps the analytical solution. However at $h = 1.99$ the solution, although stable, is far from accurate.

2.4 Implementing velocity-Verlet scheme in systems interacting with Lennard-Jones potential

To begin an in-depth analysis of MD simulations using the velocity-Verlet integration scheme, we chose a simple, commonly used potential - the Lennard-Jones potential. It is a mathematical model originally proposed for liquid argon [34], that approximates the interaction between two neutral atoms or molecules. It serves a great purpose in computational simulations as it is simple and easy to implement. We begin our discussion by first explaining the MD set up for such a simulation.

2.4.1 Lennard-Jones potential

According to the Lennard-Jones potential, for a pair of atoms i and j located at $\boldsymbol{r}_i$ and $\boldsymbol{r}_j$, the potential is given by:

$$U(r_{ij}) = 4\epsilon\left[\left(\frac{\sigma}{r_{ij}}\right)^{12} - \left(\frac{\sigma}{r_{ij}}\right)^{6}\right], r_{ij} < r_c, \tag{2.35}$$

where r_c is the interaction distance cut-off and $r_{ij} = |\boldsymbol{r}_{ij}| = |\boldsymbol{r}_i - \boldsymbol{r}_j|$, as illustrated in Fig. 2.2. The cut-off distance is used to save computation as beyond the cut-off distance the attractive force between atoms/particles is not very strong and can be ignored (or in other words is set to 0). ϵ represents the strength of the interaction and σ defines the length scale (radius of particles). The first part of the potential with power 12 can be thought of as arising from Pauli's exclusion principle, that is when atoms come too close and their electron clouds begin to overlap, there is a strong repulsive force. The other term with power 6 is an attractive tail representing a van

der Waals interaction.
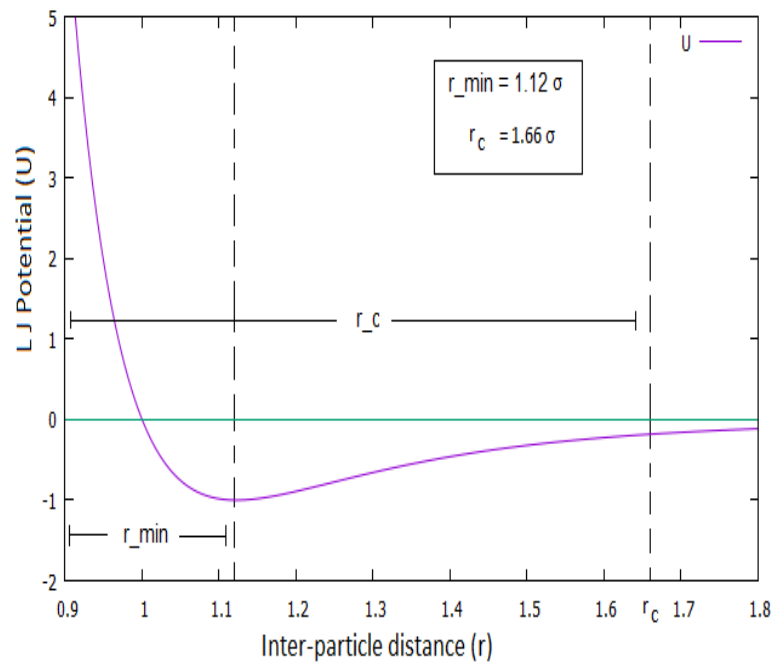
Figure 2.2: Lennard-Jones potential versus distance between two non-bonded particles. r_c represents the cut-off distance. The Fig. depicts an example where the value of $r_c = 1.66\sigma$.

The force experienced by any particle under such a potential is given by:

$$f = -\nabla U(r). \tag{2.36}$$

The force exerted on particle i by any particle j is hence given by:

$$f_{ij} = \left(\frac{48\epsilon}{\sigma^2}\right)\left[\left(\frac{\sigma}{r_{ij}}\right)^{14} - \frac{1}{2}\left(\frac{\sigma}{r_{ij}}\right)^{8}\right]r_{ij}, \tag{2.37}$$

acting along the direction $r_{ij} = r_i - r_j$, given $r_{ij} < r_c$. Also, by Newton's third law of motion $f_{ij} = -f_{ji}$.

2.4.2   MD units

In computer simulations, it is very important to keep all the physical quantities of the order unity by using dimensionless MD units. A technically correct calculation involving decimal

(floating point) numbers, can produce inaccurate results. This occurs due to poor use of finite digits that can be stored using floating point numbers. The non-significant digits in a decimal number (zeros) effectively result in the waste of digits that could have been used to store significant digits. This leaves less space for the significant digits, reducing accuracy, which inevitably results in round-off errors when algebraic operations are performed on these numbers. For example, when a small number (many orders less than unity) is multiplied by another very small number or raised to very high powers, as is the case in L-J potential equation (2.35), it can result in round-off errors that can severely affect the accuracy. We often have to deal with small numbers when performing calculation involving physical quantities in the atomic domain. Another benefit of using MD units is that some of the parameters defining the model are absorbed into the units. In case of Lennard-Jones potential, the following MD units are used :

$$\text{length} : r \rightarrow r\sigma,$$

$$\text{energy} : e \rightarrow e\epsilon,$$

$$\text{time} : t \rightarrow t\sqrt{m\sigma^2/\epsilon}.$$

The resulting equation of motion in MD units is now:

$$\ddot{\boldsymbol{r}_i} = 48 \sum_{i \neq j} \left(r_{ij}^{-14} - \frac{1}{2} r_{ij}^{-8} \right) \boldsymbol{r}_{ij}. \tag{2.38}$$

2.4.3   Simulating various phases (solid, liquid and gas) using Lennard-Jones potential and velocity-Verlet integrator

Before we start investigating properties of the velocity-Verlet algorithm used to simulate particles interacting with Lennard-Jones potential, it is worthwhile to demonstrate that the code we used (written in C++, and some data handling in python) is capable of simulating various phases correctly.

For demonstration purposes we present snapshots generated by the non-adaptive single timestep velocity-Verlet scheme. Later we will use an adaptive version of the code, which is similar to the non-adaptive version with variable timesteps and can simulate various phases in a similar fashion.

We took a two-dimensional simulation box of size 20×20, with periodic boundary conditions(PBC) in both x and y dimensions. The cut-off distance r_c for the potential was chosen to be $2.5\,\sigma$, somewhat greater than $r_{min} = 2^{\frac{1}{6}}\,\sigma$. The gaseous state was obtained using 64 particles, liquid using 256 particles and solid using 484 particles as shown in Figures 2.3 (a), (b) and (c).

This, along with other tests we have performed such as conservation of momentum and energy, suggests that our code accurately implements the Lennard-Jones potential using the velocity-Verlet integrator. Now, we can move on and start exploring merits of an adaptive velocity-Verlet scheme over the non-adaptive velocity-Verlet scheme.

2.5   Non-adaptive single timestep velocity-Verlet scheme

As stated earlier the commonly used implementation of velocity-Verlet in MD simulations is a non-adaptive single timestep velocity-Verlet scheme typically used with timestep $h = 0.007$ for L-J potentials. In MD simulations, the accuracy of integration is dependent on the ability of the scheme to be able to accurately calculate the interactions in the system at the smallest timescales. In case of Lennard-Jones potential, that directly translates to particles that are closer than σ, as the repulsive forces grow very rapidly and hence their motion needs to be integrated at a timescale small enough to accurately track the motion of such particles during a collision.

In a large enough system with a large number of particles, at any given point of time, there are generally always two particles that are close enough such that the timestep needed for the velocity-Verlet has to be really small for accuracy. Hence, although the trajectories of most of the particles in principle could be integrated with a larger timestep (resulting in faster run times of code), the system has to be evolved slowly at all times keeping up with the shortest

(a)

(b)

(c)
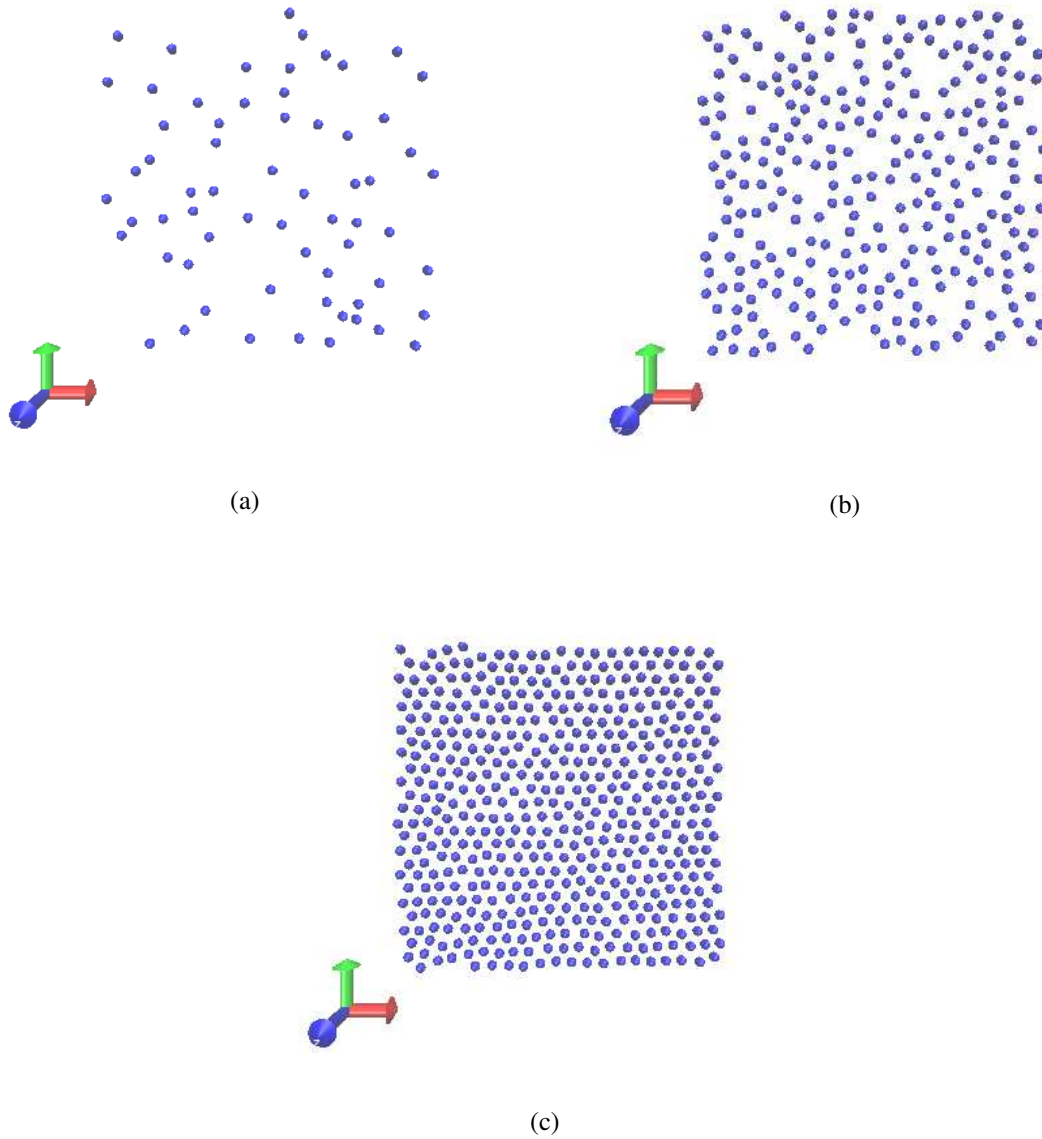
Figure 2.3: Various states (Fig. (a) - gas, Fig. (b) - liquid and Fig. (c) - solid) simulated by using Lennard-Jones potential interactions among particles in a 20×20 box. The velocity-Verlet integrator was used and PBC were applied in both dimensions.

timescales of interactions happening in the system.

One way to track the importance of these timescales is to calculate the truncation errors in position of the particles as discussed earlier in this chapter. If the truncation error exceeds acceptable values, the timestep in velocity-Verlet needs to be smaller to reduce the truncation error. We did an analysis on the truncation error of our system of size 20×20 at temprature $T = 2.0$ and at various densities to see the typical truncation error produced in the system with timestep $h = 0.007$. The $\log_{10}$ of the *maximum* truncation error at each timestep was recorded. The results are presented in Fig. 2.4.

As one would expect the truncation error is higher for higher densities as

- Collisions are more likely at higher densities

- Particles are packed closer together, closer than σ in the case of the highest densities, increasing the truncation errors.

Another thing to note is that the distribution is quite wide (more prominent in smaller 20×20 box size presented in Fig. 2.4 (a)) suggesting that many times during the simulation, the errors are quite small. This in turn suggests that the timestep could be larger as the error would increase, but still would be within acceptable accuracy. Simulations were also run using the same densities in a larger 40×40 system. As expected the truncation errors did increase which is demonstrated in Fig. 2.4. When compared to Fig. 2.4(a), one can see in Fig. 2.4(b) that the distribution for the truncation error for the same densities is now condensed towards the right and narrows, demonstrating an increase in magnitude of the typical maximum truncation errors. This is a major reason to consider an adaptive velocity-Verlet scheme, as in a sufficiently large system, one has to always use a small timestep to accurately simulate the interactions with shortest timescales in the system and hence resulting in longer run times for the simulation.
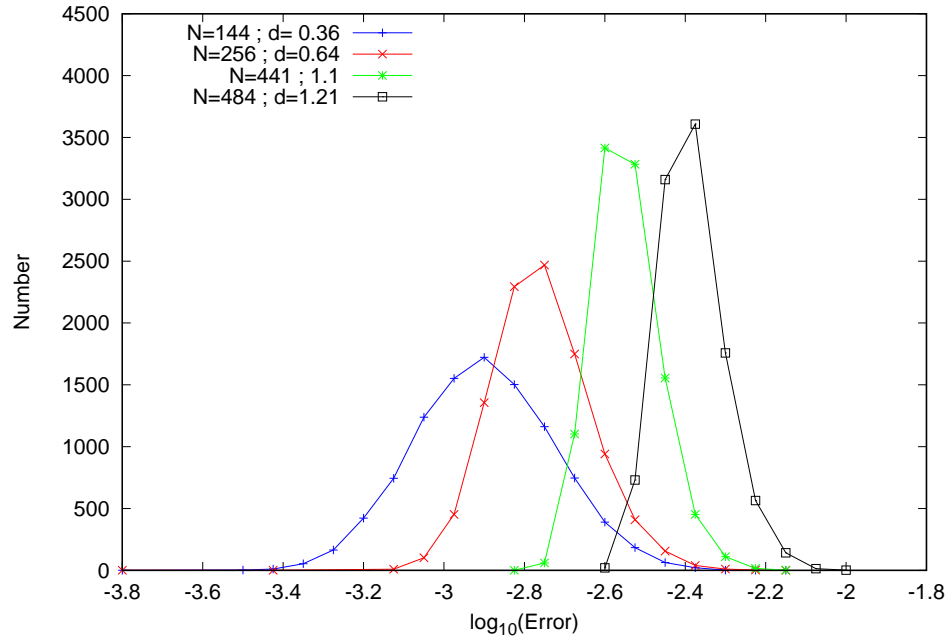
(a)
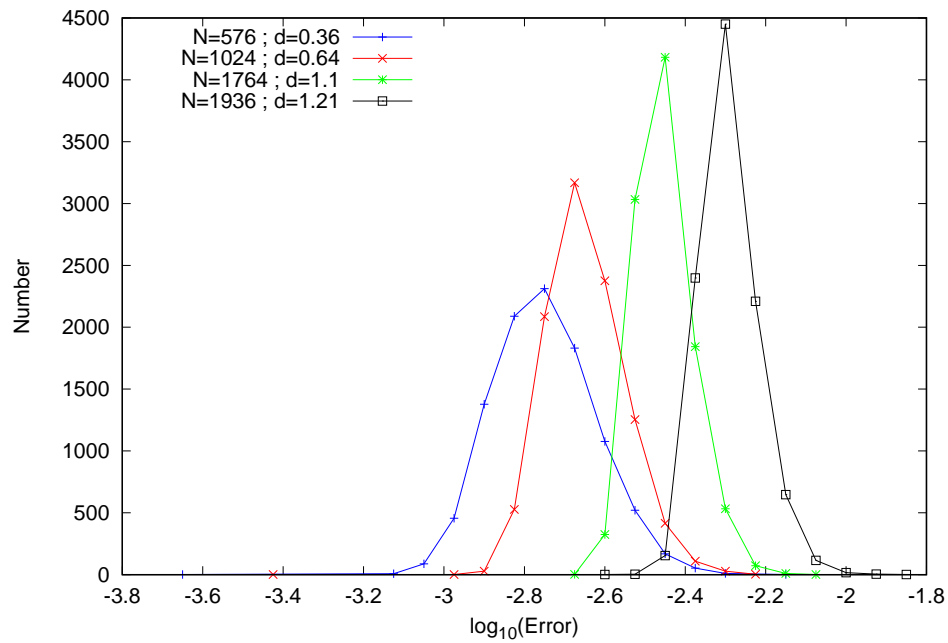
(b)

Figure 2.4: Plot of the number of times a maximum truncation error occurs during a non-adaptive single timestep (0.007) simulation versus the maximum truncation error, for box sizes 20×20 (Fig. a) and 40×40 (Fig. b) at various densities. All simulations were run for a total time of $t = 10000 \times 0.007$. N represents the number of particles and d is the particle density.

2.6   Adaptive single timestep velocity-Verlet scheme

Due to the poor run-time performance of the non-adaptive STS scheme as discussed in the above section, the need for an adaptive velocity-Verlet scheme is pretty clear. Adaptive means that the value of the timestep (h) can be changed at every step. Under such an scheme, during the steps in the simulation when the truncation error is lower than a prescribed tolerance, the value of h can be increased and when the truncation error is higher than the prescribed tolerance, the value of h can be decreased. This way the scheme is not wasting time making more accurate calculations than needed and results in faster run times. Although this would not be as effective as our ultimate end goal - a multiple timestep adaptive scheme, it should still result in some performance gain over a non-adaptive single timestep scheme. It is worth noting however that similar approaches are used in some popular schemes, for example RKF45 [5] (Runge-Kutta-Fehlberg), an adaptive Ordinary Differential Equation (ODE) solver.

In our adaptive code, we actually move the system one step in time in order to calculate and store the error in the particles' positions, the new positions are then discarded and all the particles are moved back in time to the previous step. The maximum of all truncation errors is then used to determine the appropriate timestep size to be used to move the simulation to the next step in time. This approach, however, leads to some waste of computation, to get around this issue, we devised an additional control along with the error tolerances called the stability criteria. Our main goal here is to evaluate the effective potential performance of such a scheme, not necessarily to fully optimize its performance.

There are five controls (four active, one passive) for the adaptive STS (Single Time Step) velocity-Verlet scheme. The active controls were used to control the simulation whereas the passive control was demonstrated to be equally effective if one chooses to use it, but was not used. The controls are listed below:

1. **MIN_STEPSIZE (active)** : Minimum possible value of timestep h.

2. **MAX_STEPSIZE (active)** : Maximum possible value of timestep h.

3. **MINERR (active)** : Minimum value allowed for $\log_{10}$ of maximum truncation error tolerance at each step.

4. **MAXERR (active)** : Maximum value allowed for $\log_{10}$ of maximum truncation error tolerance at each step.

5. **H_STABLE (passive)** : Maximum value allowed for timestep h so that the simulation is stable.

For our code, we first ran the non-adaptive code and calculated the mean (μ) and standard deviation (σ^*) (not to be confused with inter-particle distance represented by σ) of $\log_{10}$ of maximum truncation error at each timestep for simulation with fixed h=0.007 as plotted in Fig. 2.4 in previous section. We then set our controls as follows :

$$MINERR = \mu$$
$$MAXERR = \mu + 2 * \sigma^*$$

We changed the value of h by a factor of 2 or 1/2 when increasing or decreasing the step-size. We let the controls for h (MIN_STEPSIZE and MAX_STEPSIZE) to be practically un-bounded(a very wide range). The control for stability H_STABLE was calculated according to the description in the following section but was not used. Given the adaptive nature of the code, one would expect to see the values of h getting smaller for larger densities. We tested this assumption for box sizes 20×20 and 40×40 and the results are presented in Fig. 2.5. Notice the large width of the distribution at lower densities, indicating that the timesteps can indeed be significantly higher than 0.007 (typically used value in non-adaptive STS scheme). The distribution is wider for smaller box size 20×20 than for the larger box size 40×40 at the same densities, this is due to the fact that in a larger box size with more particles there are more collisions, driving down the timestep size needed for the same simulation (the same control values were used for both box sizes at all densities). Notice how the values of the h get smaller with both larger density, and larger box size. It can be seen that the shift is most dramatic for the lowest density systems.
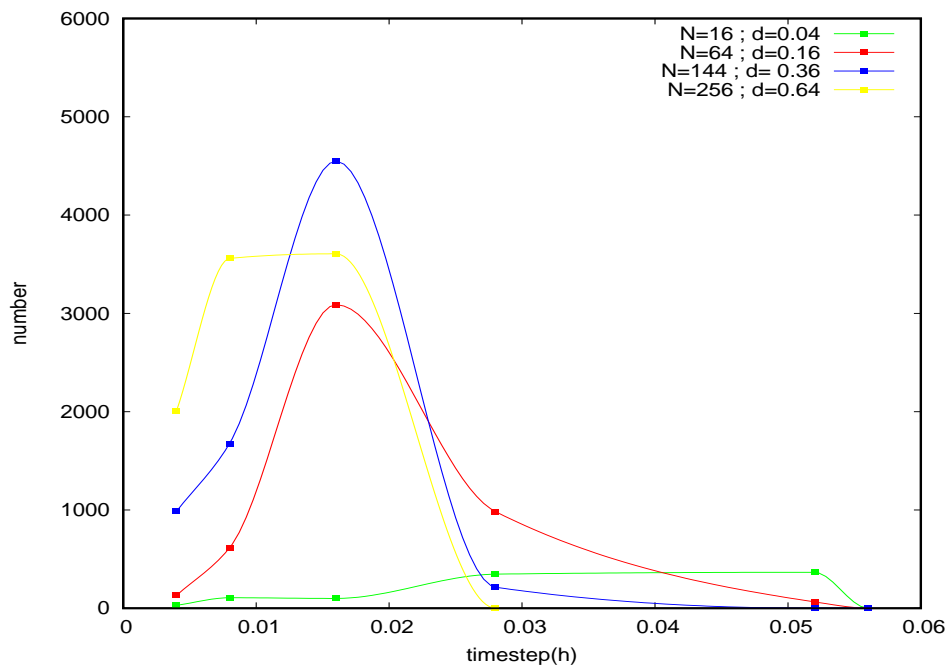
(a)
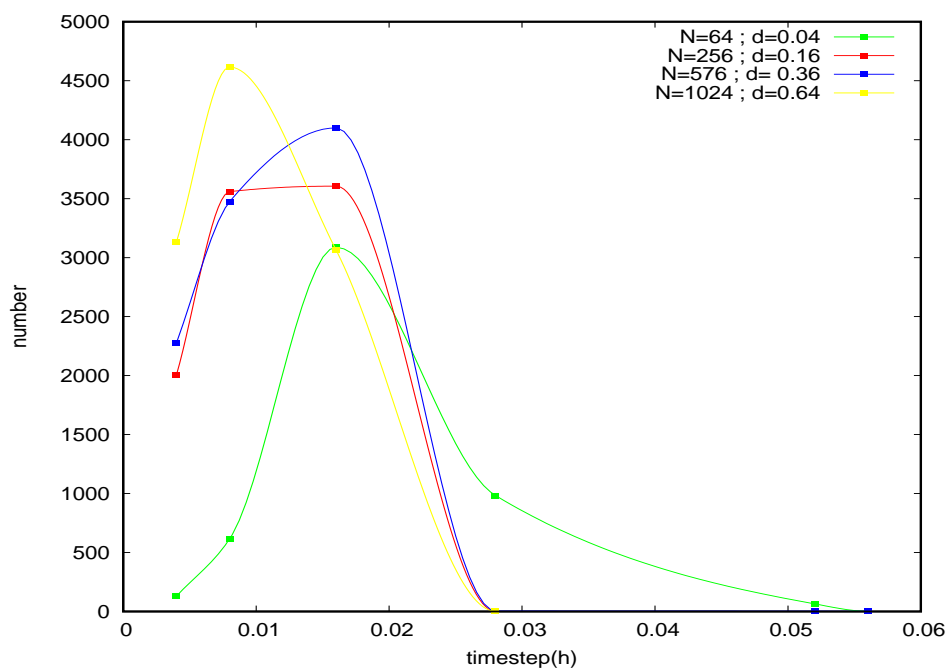
(b)

Figure 2.5: Plot of number of times the timestep(h) value was used during an adaptive single timestep simulation versus the timestep values for box sizes 20×20(Fig. a) and 40×40 (Fig. b) at various densities. All simulations were run for a total time of $t = 10000 \times 0.007$. N represents the number of particles and d is the particle density.

2.7   Stability criteria for Lennard-Jones simulation using velocity-Verlet

As discussed in section 2.3 the stability condition for a single particle motion under a harmonic force was given by equation (2.32),

$$h < \frac{2}{\sqrt{k}}. \tag{2.39}$$

Let us consider a system using Lennard-Jones potential for the interaction between particles. Without loss of generality, let us assume that the mass of the particle is equal to 1 ($m = 1$) and $\epsilon = 1$. This is equivalent to setting units. The force in MD units acting on any particle is given by:

$$\ddot{r}_i = 48 \sum_{i \neq j} \left(r_{ij}^{-14} - \frac{1}{2} r_{ij}^{-8} \right) r_{ij}. \tag{2.40}$$

When the particle is moved by a small distance δr, the force acting on the particle is then given by taking a Taylor's expansion about r.

$$(r_i \ddot{+} \delta r) \approx F_k + \delta r \frac{\partial}{\partial r_i} \ddot{r}_i, \tag{2.41}$$

where F_k is a constant force. Higher order terms of δr are ignored as δr is small. This is effectively of the form of a harmonic force given by:

$$F = F_k + k_{eff} x, \tag{2.42}$$

where the displacement $x = \delta r$ and effective k given the harmonic form of the force is $k_{eff} = \frac{\partial}{\partial r_i} \ddot{r}_i$.

Hence the stability criteria using analysis done for the harmonic force can be used, and this gives us the stability criteria,

$$h < \frac{2}{\sqrt{k_{eff}}}, \tag{2.43}$$

where

$$k_{eff} = 48 \sum_{i \neq j} \left(-13 r_{ij}^{-14} + 3.5 r_{ij}^{-8} \right). \tag{2.44}$$

When there are multiple particles in the system the value of h is constrained by the $\max(k_{eff})$ of all the particles.

$$h < \frac{2}{\sqrt{max(k_{eff})}} \tag{2.45}$$

2.7.1 Testing the stability criteria

The stability criteria stated above was tested for the adaptive version of the scheme. The testing was done on different densities and with box sizes 10x10, 20×20 and 40×40. The adaptive increment condition for *h* was limited to only one consecutive increment at a time i.e if the system's maximum truncation error is smaller than error tolerance for several consecutive steps, the value of *h* can not be increased (doubled) for any two consecutive steps. Such restriction was placed to avoid rapid increase in timesteps which were seen to be unable to come down soon enough when the maximum truncation error of system goes down rapidly. No restriction was placed on reducing the *h* values.

The results for 20×20 box size simulations for 16 and 64 particles, with temperature 2.0, are shown in Figures 2.6 and 2.7, respectively. The stability criteria calculated at every timestep according to equation (2.45) is shown in green, the actual adaptive timestep value (*h*) is shown in blue and the commonly used timestep value for velocity-Verlet scheme 0.007 in shown in black line with stars on it.

Notice how the *h* values adjust in response to truncation error tolerance and always remain lower than the value required by the stability criteria. The dips in stability criteria correspond to collisions between particles which decreases the maximum truncation error of the system, in turn reducing the value of adaptive timestep *h*. It can be clearly seen that the stability criteria which was used as a passive control could be an effective control, and can indeed be used to

Figure 2.6:   Plot of Stability criteria per timestep (in green), actual adaptive timestep h (in blue) and commonly used timestep=0.007 for velocity-Verlet integrator, with 16 particles in a 20×20 box. Inset: a zoomed out version of the same plot.

check if a simulation is stable given the truncation error tolerance and adaptive timestep value constraints.

2.8 Multiple Timestep (MTS) Adaptive velocity-Verlet Scheme

Although the single timestep adaptive velocity-Verlet scheme does have performance gains when compared to a non-adaptive single timestep velocity-Verlet scheme, the gain is quickly diminished if the densities are large or the system size is big enough. Hence, it becomes important that all particles in a system are not constrained by the fastest phenomenon (shortest timescale) in the system. If, for example, two particles are colliding in the system, the forces acting on them are way larger than the forces on rest of the particles, and hence they need to be integrated with smaller timesteps for results to be within acceptable accuracy. This generates a need for an adaptive integration scheme that can accommodate multiple timescales.

2.8.1 RESPA and Reversible Multiple Timescale Molecular Dynamics

Although just using the LJ potential in our system leads to various timescales, depending upon distance between particles, in other MD simulations, the separation of timescales can be quite complicated. A MD simulation might have several potentials acting on the particles within the system, for example:

$$F(x) = F_{bond}(x) + F_{dihedral}(x) + F_{electrostatic}(x) + F_{vanderWaals}(x). \tag{2.46}$$

Each force mentioned above might have an inherent time scale and all forces combined may cover a very wide range of timescales. In such a scenario, with huge separation of timescales, integrating the largest timescale phenomenon using the shortest timescale, might produce very accurate results, but is often unnecessary and slows down the simulation. For example, in a worst case performance scenario for single timestep schemes, one might have just one potential that produces timescales orders of magnitude lesser than the rest of the potentials and the
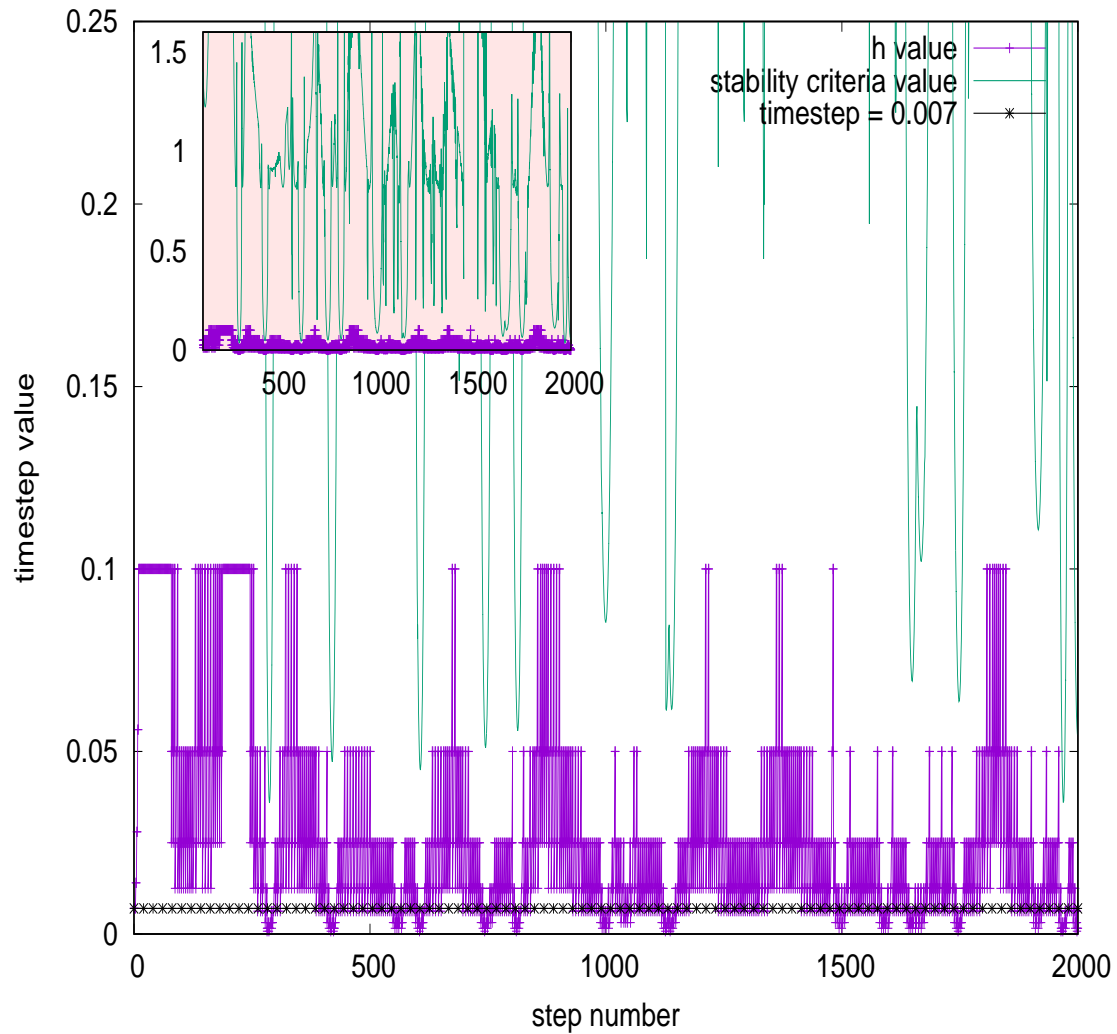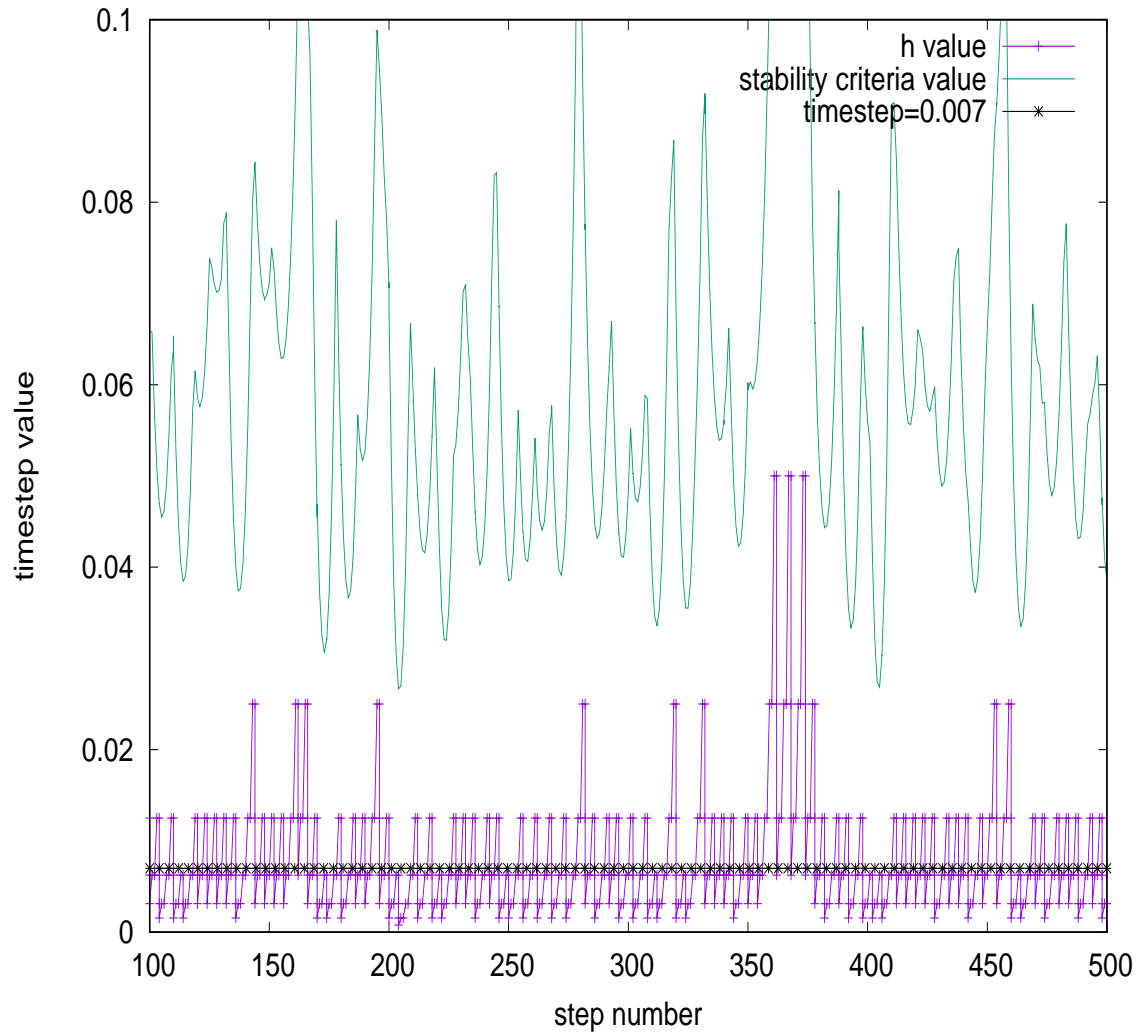
Figure 2.7: Plot of stability criteria per timestep (in green), actual adaptive timestep h (in blue) and commonly used timestep=0.007 for velocity-Verlet integrator, with 64 particles in a 20×20 box. Only a few steps and limited values of timesteps up to 0.1 were plotted to clearly show the adaptability of h with respect to stability criteria.

system would still need to be integrated using a very small value for timestep, severely slowing down the simulation.

To combat this inherent timescale issue in MD simulations, it is beneficial to formulate the integration schemes that include multiple timescales. These schemes are referred to as MTS (Multiple timestep schemes) and have become increasingly popular in MD simulations [8], [31]. One of the algorithms called RESPA (Reversible Reference System Propagator Algorithm) due to Tuckerman et al [31], is of particular interest to us as it can be implemented using the velocity-Verlet integrator [30]. RESPA can be used in systems with multiple potentials acting at different timescales(see [31] for details). It can also be used to generate multiple timescales for a single potential with both short and long range components.

For example, in a Lennard-Jones potential, there are two components - short range (Pauli's exclusion) and intermediate range (van der Waals). Under RESPA forces due to such a potential are broken in to a short range force $F_s(x)$ and a long range force $F_l(x)$ using a switching function $S(x)$:

$$F(x) = S(x)F(x) + [1 - S(x)]F(x), \tag{2.47}$$

where,

$$F_s(x) = S(x)F(x), \tag{2.48}$$

and

$$F_l(x) = [1 - S(x)]F(x). \tag{2.49}$$

The switching function can be any function that *switches* from 1 to 0 at some inter-particle distance r_0. In other words the switching function switches the force $F(x)$ from $F_s(x)$ at short range ($r < r_0$) to $F_l(x)$ at long range ($r \geq r_o$).

Under such a scheme, the long range forces are applied every $\Delta t = n * \delta t$ and short range forces are applied every δt. This saves computation time and results in faster MD simulations with comparable accuracy.

Although this discussion explains the case of potentials that can be broken down in to two - short range and long range components, similar approach results can be used for multiple

potentials with separation of timescales. We accomplish this by treating the particles that experience the largest forces as if they were acted upon by a *short-range forces*, and the rest of the particles are assumed to be acted upon by *long-range forces*.

2.8.2 MTS velocity-Verlet algorithm

The MTS(RESPA) version of the velocity-Verlet algorithm is different from what we had implemented in the non-adaptive and adaptive STS versions of the code. For a system that has multiple potentials that result in forces acting at different timescales, the algorithm is described below.

Let's assume the long range forces or the forces requiring time steps larger than the smallest timestep are represented by F_p (deviation forces) and short range forces or the forces requiring smallest timestep are represented by F_r (reference forces). The mass of all the particles is assumed to be *m* for simplicity.

It is obvious that in the case of multiple potentials the deviation forces have several contributors and characteristic timesteps corresponding to the forces. For purpose of demonstrating the algorithm via pseudo-code, lets assume it has P deviation force contributors. In such a scenario, the deviation forces on a particle i is given by:

$$F_p(i) = \sum_{k=1}^{k=P} F_k(i). \tag{2.50}$$

Each of these deviation forces $F_k(i)$ has their own timescale $\Delta t_k(i)$ such that $\Delta t_1(i) = n_1 \Delta t_2(i)$, $\Delta t_2(i) = n_2 \Delta t_3(i)$, $\Delta t_3(i) = n_3 \Delta t_4(i)$, ... ,$\Delta t_{P-1}(i) = n_{P-1} \Delta t_P(i)$. In our MTS simulations (discussed in next section), we have restricted the timesteps(Δt_k) to be a factor of 2^a of each other (a simple, commonly used choice), where *a* can be negative, resulting in $\Delta t_k(i) = 2^a \Delta t_{k+1}(i)$.

The algorithm for MTS(RESPA) velocity-Verlet due to Tuckerman *et al.* [30] is explained in Algorithm 1. The term force pair used in Algorithm 1 refers to the two particles interaction (represented as (a,b)), which means that particle a is being acted upon by the force due to particle b. Each force pair is assigned a timestep depending on the timestep distribution of

the particles in the system. Each particle forms a force pair with all other particles sharing the same or a smaller timestep value.

Let's explore an example based on the algorithm discussed above. Let's assume that at any given time in a simulation of a 6 particle system interacting with LJ potentials, the timestep distribution looks like:

Table 2.1: A MTS example case

Timestep required	Particle ID	Corresponding force pairs
T	1,2	(1,2), (2,1), (1,3), (1,4), (1,5), (1,6), (2,3), (2,4), (2,5), (2,6)
T/2	3,4	(3,4), (4,3), (3,5), (3,6), (4,5), (4,6)
T/4	5,6	(5,6), (6,5)

If this system has to be moved to the next T unit in time, the way the RESPA velocity-Verlet will move the system forward has been described in Fig. 2.8. The force pairs reduce the number of times we need to calculate the force acting on a particle as the particles do not have force pairs with a particle with larger timestep. For example, in our example case, the force acting on particle 4 can be calculated by looking up all the force pairs that have the first particle as 4 (instead of having to calculate forces on 4 due to all other particles in the system). The performance(run time) advantage of the RESPA can be understood by the following two major points :

- **Less steps:** At one given step, the entire system can be moved ahead by T_{max} (the largest of the timesteps required by any of the particles). To put this in perspective, in adaptive STS scheme we were moving the entire system ahead in time by T_{min} (the smallest of the timesteps required by any of the particles), which still had some performance advantage over the non-adaptive scheme. It is clear MTS can move the simulation to any given time in less steps (i.e. fewer force calculations) than the adaptive STS scheme.

Algorithm 1 RESPA velocity-Verlet

1: $\dot{q} = \dot{q} + \frac{\Delta t}{2m} F_P$ ▷ update velocities half a step for all force pairs requiring largest timestep

2: **DO** iPM1 = 1,nPM1 ▷ Do for 1 through $n = \frac{current\ timestep}{next\ smallest\ timestep}$

3: $\dot{q} = \dot{q} + \frac{\Delta t_{P-1}}{2m} F_{P-1}$ ▷ update velocities half a step for all force pairs requiring largest timestep

4: ....

5: **DO** i1 = 1,n1

6: $\dot{q} = \dot{q} + \frac{\Delta t_1}{2m} F_1$ ▷ update velocities half a step for all force pairs requiring second smallest

   timestep

7: **DO** i = 1,n ▷ Do for 1 through $n = \frac{second\ smallest\ timestep}{smallest\ timestep}$

8: $\dot{q} = \dot{q} + \frac{\Delta t}{2m} F_r$ ▷ update velocities half a step for all force pairs requiring smallest timestep

9: $q = q + \Delta t \dot{q}$ ▷ update position one step for all force pairs requiring smallest timestep

10: **CALL FORCE_r** ▷ Calculate reference forces

11: $\dot{q} = \dot{q} + \frac{\Delta t}{2m} F_r$

12: **ENDDO**

13: **CALL dFORCE_1**

14: $\dot{q} = \dot{q} + \frac{\Delta t_1}{2m} F_1$

15: **ENDDO**

16: ....

17: **CALL dFORCE_(P-1)** ▷ Calculate deviation forces acting at timescale Δt_{P-1}(second largest

   timestep)

18: $\dot{q} = \dot{q} + \frac{\Delta t_{P-1}}{2m} F_{P-1}$ ▷ update velocities half a step for all force pairs requiring second largest

   timestep

19: **ENDDO**

20: **CALL dFORCE_P**

21: $\dot{q} = \dot{q} + \frac{\Delta t}{2m} F_P$ ▷ update velocities half a step for all force pairs requiring largest timestep

---

- **Time complexity:** Each particles interacts with less than (N-1) particles, reducing the time complexity from $O(N^2 - N)$ to a lesser order depending on the timestep distribution of the system.

2.9 LJ simulation using adaptive MTS velocity-Verlet scheme

After going through the last section, at this point readers might wonder if there is any merit in implementing an already existing scheme or what exactly are we doing differently that adds value? The answer is that the RESPA algorithm proposed by Tuckerman et al. ([30]) is not adaptive in nature. That means, the user has to choose the timesteps to be used for various potentials' interactions in a simulation beforehand. This seriously limits the performance gains of the non-adaptive MTS scheme. Our work implements an *adaptive* MTS scheme, that choses timestep values for each particle at each timestep (depending on user defined truncation error tolerance) dynamically during the simulation.

Earlier in the chapter, for the simulations performed using adaptive STS velocity-Verlet scheme, the distribution of timesteps was depicted in Fig. 2.5. The advantage of using a MTS adaptive velocity-Verlet scheme is that in principle, irrespective of the density of the system or the box size, the distribution of timesteps should not shift as in the adaptive STS scheme. This is due to the fact that in a adaptive MTS scheme, for timestep selection for each particle we are not restricted by the largest truncation error in the system. We select a timestep for each particle either based on their own truncation error estimate and user defined truncation error tolerance, or by using stability criteria, or some other suitable control.

We ran simulations for box sizes 20×20 and 40×40 for various number of particles using the MTS adaptive velocity-Verlet scheme. The particles interacted with each other using the LJ potential and all parameters (σ etc.) were set to the same values as the ones used in the adaptive STS version of the simulations described earlier in this chapter. The mechanism for choosing the timestep values for all the particles was the same as well, although in these simulations each particles' timestep value was calculated independently, instead of a single timestep value
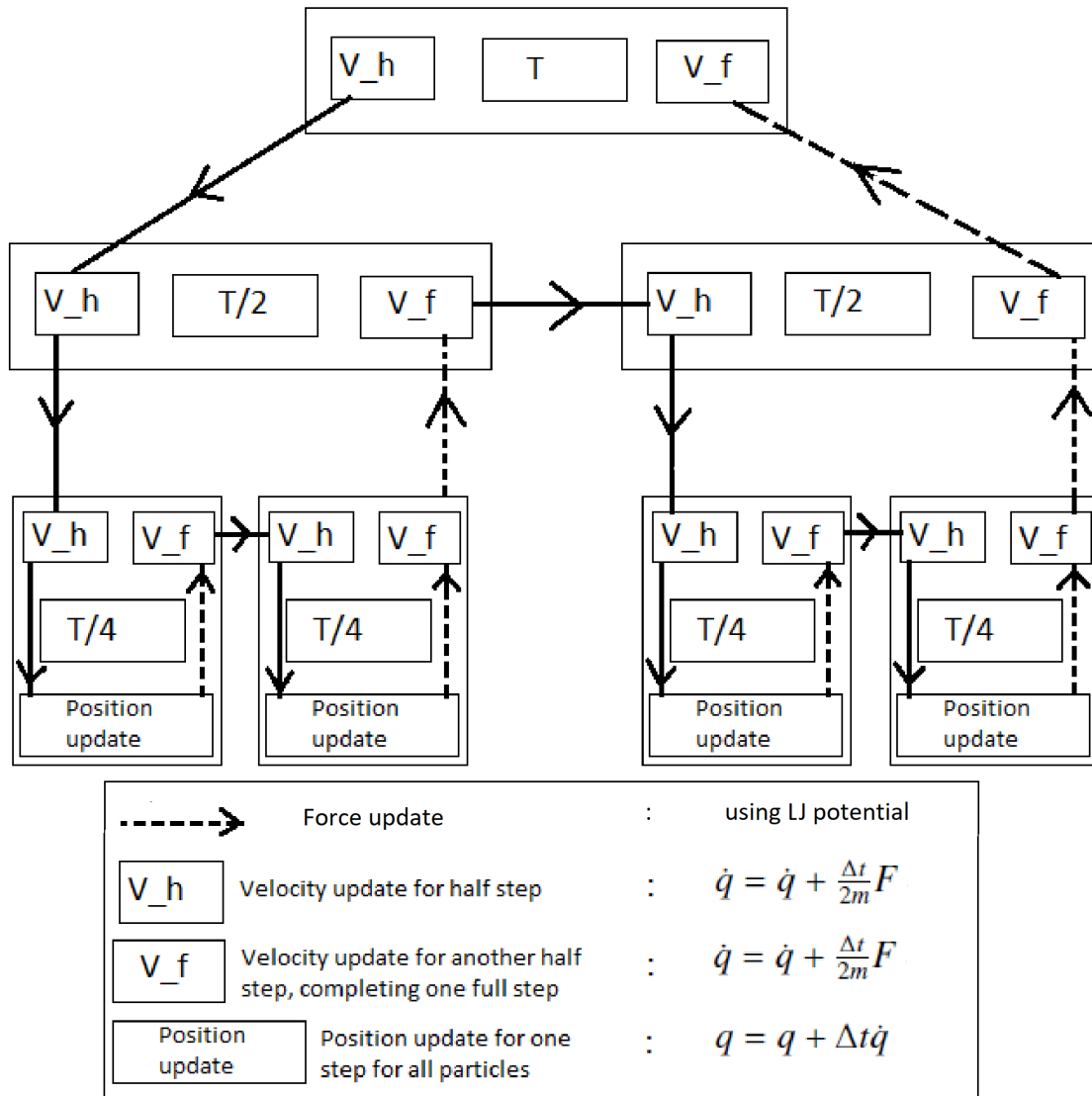
Figure 2.8: A pictorial depiction of the example case mentioned in table 2.1 describing the working of RESPA velocity-Verlet scheme.
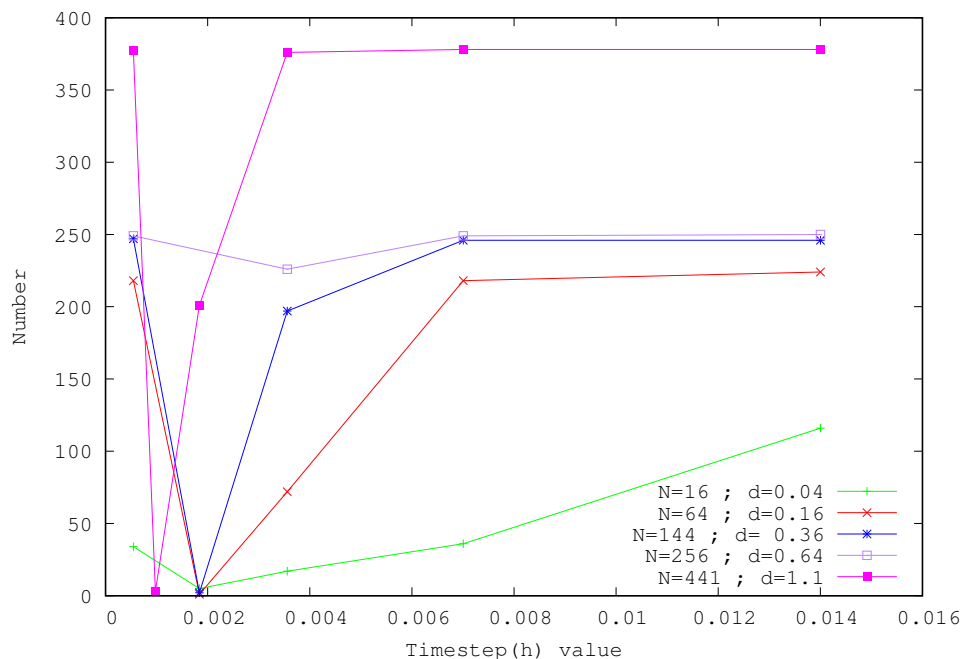
(a)
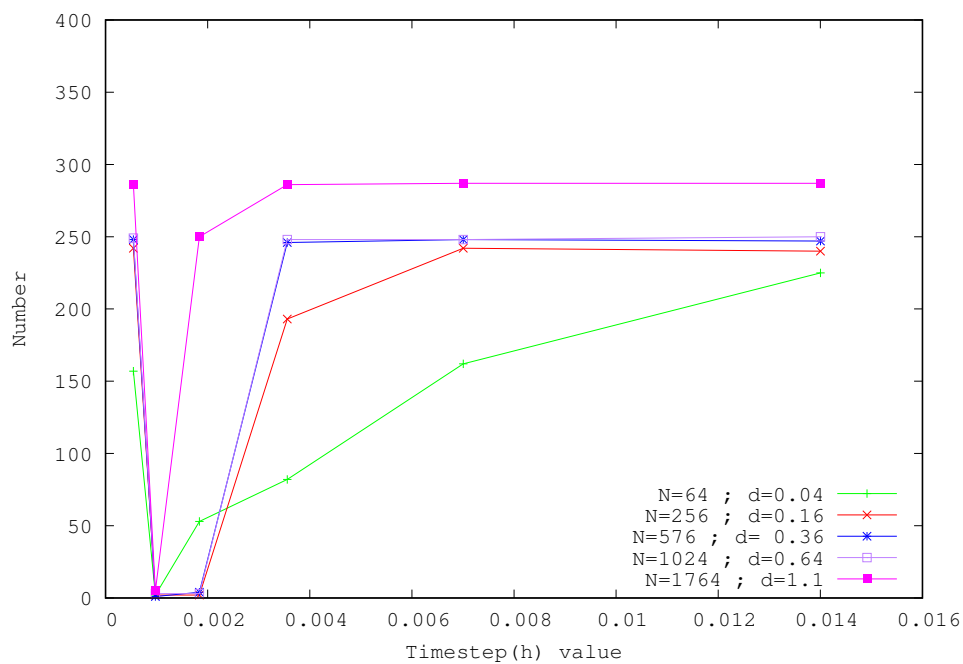
(b)

Figure 2.9: Plot of number of times timestep (*h*) value was used during adaptive MTS simulation versus the timestep values for box sizes 20×20(Fig. a) and 40×40(Fig. b) at various densities. All simulations were run for a total time of $t = 1000 \times 0.007$. N represents the number of particles and d is the particle density.

for the entire system. The result of the distribution of timesteps in the MTS simulations can be seen in Fig. 2.9.

In Fig. 2.9, we can see that, unlike the plots for the timestep distribution in adaptive STS version of the simulations (shown in Fig. 2.5), there is no shift in the distribution when varying densities within same box size or at same densities at different box sizes. This clearly demonstrates that the adaptive MTS version is able to set a timestep value for all particles separately depending on their respective truncation error and user supplied truncation error tolerance, hence resulting in faster simulations than the adaptive STS version of the scheme which uses the same timestep for all particles.

2.10   Conclusion

From the discussion in this chapter, it is evident that the non-adaptive velocity-Verlet scheme is slower and less efficient than the adaptive STS scheme. The adaptive STS scheme in turn is slower than the adaptive MTS scheme. We have demonstrated that the MTS scheme can be implemented in an adaptive manner such that the timestep per particle can be chosen depending upon some suitable control. We demonstrated that the control can be the truncation error in the position, or the stability criteria introduced earlier in this chapter. At the time of writing this thesis, we are still working on evaluating the extent of the performance gains (including run times), and expect to present that and other analyses in the form an article in the future.

Chapter 3

Elastic Driven Sphere in Newtonian Fluid

3.1 Introduction

Microscopic particles/swimmers have found increasingly many applications in biological, chemical and physical sciences. The Scallop Theorem plays a vital role in understanding and explaining the behavior of any such driven swimmer. It simply states, as explained in Chapter 1, that a micro-swimmer cannot propel itself using reciprocal motion in a Newtonian fluid.

One can understand this observation more carefully using the Navier-Stokes equation. For irrotational fluid flow, the equation of motion reads [29]:

$$\rho\frac{\partial \boldsymbol{v}}{\partial t} + \rho(\boldsymbol{v} \cdot \boldsymbol{\nabla})\boldsymbol{v} = -\boldsymbol{\nabla} p + \eta\boldsymbol{\nabla}^2\boldsymbol{v}, \tag{3.1}$$

where p is the pressure field describing the fluid, ρ is the density, v is the velocity and η is the shear viscosity. For small Reynolds number Re (eq. (1.1)), the terms $\rho(\boldsymbol{v}.\boldsymbol{\nabla})\boldsymbol{v}$ and $\rho\frac{\partial \boldsymbol{v}}{\partial t}$ should become negligible as inertial forces are negligible compared to viscous forces, and the equation reduces to [29]:

$$\eta\boldsymbol{\nabla}^2\boldsymbol{v} = \boldsymbol{\nabla} p. \tag{3.2}$$

The relative insignificance of inertial terms, ($\rho(\boldsymbol{v}.\boldsymbol{\nabla})v$ and $\rho\frac{\partial \boldsymbol{v}}{\partial t}$) can be explained by the following example. If we have an object with characteristic size L, moving in some oscillatory

manner with period T and characteristic velocity v, then the order of magnitude of the terms in Eq.(3.1) is:

$$
\begin{aligned}
\left| \rho \frac{\partial \boldsymbol{v}}{\partial t} \right| &\sim \rho \frac{v}{T}, \\
|\rho (\boldsymbol{v} \cdot \boldsymbol{\nabla}) \boldsymbol{v}| &\sim \frac{\rho v^2}{L}, \\
\left| \eta \boldsymbol{\nabla}^2 \boldsymbol{v} \right| &\sim \frac{\eta v}{L^2}.
\end{aligned}
\tag{3.3}
$$

Now, since the fluid flow is driven by ∇p, it is guaranteed not to be negligible. If the *Reynolds Number*, the ratio of inertial forces to viscous forces,

$$
Re = \frac{\rho v L}{\eta},
\tag{3.4}
$$

and the *Stokes Number*, the ratio of the unsteady $\partial u / \partial t$ term to viscous forces,

$$
\mathcal{S} = \frac{\rho L^2}{\eta T},
\tag{3.5}
$$

are both small then the terms $\rho \frac{\partial \boldsymbol{v}}{\partial t} + \rho (\boldsymbol{v} \cdot \boldsymbol{\nabla}) \boldsymbol{v}$ should become negligible (note that under the common assumption that $v \sim L/T$, $\mathcal{S} = Re$). In that case the equation reduces to Stokes equation[29]

$$
\eta \boldsymbol{\nabla}^2 \boldsymbol{v} = \boldsymbol{\nabla} p.
\tag{3.6}
$$

Under this simplified relationship, the fluid flow loses its time-dependence and depends only on the pressure gradient and the imposed boundary conditions. For rigid objects suspended in a fluid (which can be viewed as a kind of boundary condition), this amounts to the statement that the evolution of the system depends only on the path through the configuration space, and thus since a body undergoing reciprocal motion will retrace its path through the configuration space periodically, it can achieve no propulsion. We show later in this chapter that this is not always true, as the underlying assumptions are never really completely valid.

In this chapter we construct and drive an flexible spherical swimmer in a water-like fluid. We then discuss the results and compare them to theoretical models.
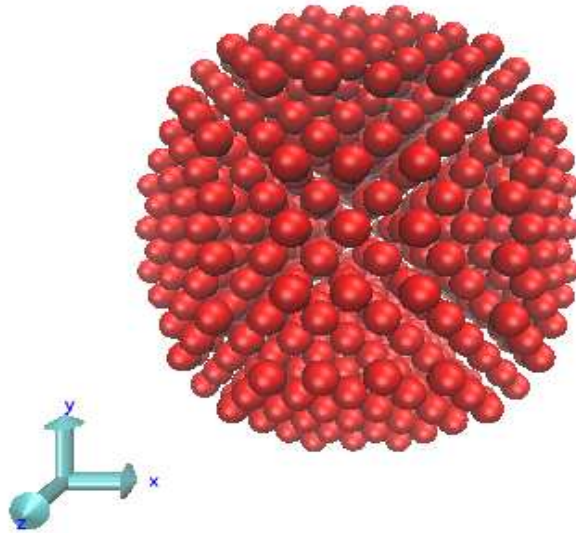
Figure 3.1: Sphere with hcp lattice structure.

3.2 Model

When modeling an object at microscopic length, it is a natural choice to choose a spherical shape as it represents most of the globular matter found at such length scales in biological systems. For our simulation, we constructed such a spherical elastic swimmer in LAMMPS [21]. The details of the construction of the swimmer, the driving model, results and its detailed analysis are covered in the sub-sections ahead.

3.2.1 Elastic spherical swimmer

The driving scheme requires the swimmer to be constructed in such a way that the length of the bonds connecting atoms can be varied sinusoidally. As a result the sphere was made of particles in a hexagonally close packed (hcp) lattice connected with harmonic bonds. The sphere can be seen without the harmonic bonds in Fig. 3.1 and with harmonic bonds in Fig. 3.2.

The sphere is made up of 856 particles, and tests were conducted for elastic spheres with diameter 4 μm and 10 μm. The outermost particles form a shell or layer that is used to interact
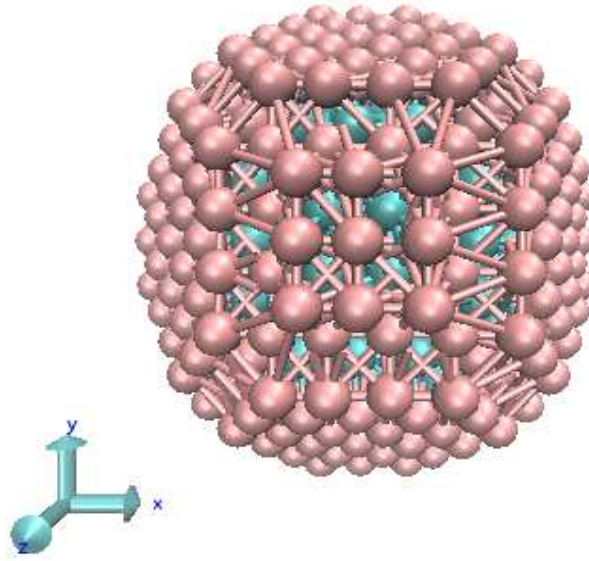
Figure 3.2: Sphere with hcp lattice structure and harmonic bonds. The outermost particles form a layer that interacts with the lattice-Boltzmann fluid.

with the fluid which is simulated by using the lattice-Boltzmann method(LBM). Hydrodynamic forces are added to the outer layer of particles using the lb/viscous [15] fix in LAMMPS that lets fluid simulated by LBM interact with MD particles [14] [18].

Each particle is connected to six neighbors, three on each side of their Y-Z plane. The potential function for the harmonic bond between particles is given by:

$$V(r) = \frac{1}{2}k(r - r_0)^2,$$
(3.7)

where, k is harmonic bond coefficient, r is the distance between the particle and its neighbor and r_0 is the equilibrium inter-particle distance. We can use standard analysis of harmonic crystals [2], to determine the elastic bulk modulus B of such a hcp crystal, which is given by the relation:

$$B = \frac{\sqrt{8}}{3}\frac{k}{r_o}.$$
(3.8)

To show a range of behavior and to show that the elastic sphere exhibits different behavior

at different elasticity, we conducted tests using elastic bulk moduli B = 1.88 kPa and B = 18.8 kPa. These values are similar to bulk moduli values for muscle tissue [4] on the high end and to liver tissue [35] on the lower end. Reynolds number for the swimmers in our simulations were in the range of 10^{-2} to 10^{-4}.

The mass of the constituent particles was set in such a way that the entire density of the sphere is 1 gm/cm^3, which was the density of the fluid in the system, hence making the sphere neutrally buoyant. This puts the mass of 10 μm diameter sphere around 0.524 ng, which is comparable to an average E. Coli bacterium [13].

3.2.2 Driving scheme

In order to propel the sphere forward, a driving scheme was devised that varies the bond length between the constituent particles periodically. This produces vibrations that closely resemble the behavior of piezoelectric materials under external electric fields [12] and makes sure that such a scheme is practically viable. The sphere was divided into two halves along the Y-Z plane orthogonal to one of the 6 hcp lattice directions. All bonds in one half with bond length $r_{0,i}$ ($r_{0,1}$ for one half and $r_{0,2}$ for the other) were then varied sinusoidally via the following relation:

$$r_{0,i}(t) = L(\alpha + (1 - \alpha)sin(\omega t + \phi_i)). \tag{3.9}$$

Here L is the natural bond length, $\alpha \in [0.75, 1]$, making αL the average bond length upon stimulation, $|\phi_2 - \phi_1| = \pi$. As a result of such a driving scheme, the equilibrium bond lengths would vary sinusoidally from a maximum value of L to a minimum value of $(2\alpha$-1)L, and the variation in both halves would be out of phase by π radians. We tested the sphere motion with different values of α. The motion of the sphere during one period is shown in Fig. 3.3. The sphere starts at equilibrium in state (a), the right half expands and left half contracts in state (b), the right half further expands and left half further contracts in state (c), right half begins to shrink and left half begins to expand in state (d), right half further shrinks and left half further expands in state (e), finally in both halves return to equilibrium state in state (f).

It should be noted that the halves of the sphere are not exactly symmetric as there are slightly more particles on the right half of the sphere as the bonds crossing the mid-plane are assigned to right side. Hence, the right side of sphere(red colored) in Fig. 3.3 is slightly bigger than the left side(blue colored). This results in a motion that is not exactly symmetric. As a result of this slight asymmetry, the sphere picks up a drift in one direction breaking symmetry and *"walks"* like an off-balance washing machine walking across the floor.

3.3   Results

The center-of-mass motion of the sphere is a wave pattern about its direction of velocity as shown in Fig. 3.4, as expected under our driving scheme. The effectiveness of a driving scheme can be understood by looking at the velocity of the swimmer. We measured the average velocity of the sphere v_{avg} as a function of the oscillation period τ for $\alpha = 9/10$ (10 % variation in bond length).

We ran simulations for two spheres, with diameter 4 μm and 10 μm. Each sphere was also tested with bulk moduli values B = 1.88 kPa and B = 18.8 kPa. Each dataset contained 110 simulations each corresponding to a different frequency ranging from 0.2 μs to 256 μs. The simulation run time was equal to 150 times the driving period for each sphere. Since the sphere takes some time to gain a stable drift along its direction of velocity, we chose to sample the last 10 periods when calculating v_{avg}. We tested the velocities averaged over variable periods and starting at variable times. After testing for a large number of values of start and end times and averaging period, we found that measuring v_{avg} from the 140th period until the 150th period was reasonably precise as the velocity converges to a stable value after such a long time period. The results for v_{avg} analysis are shown in Fig. 3.5.

It can be seen that for short periods, there are many peaks which correspond to internal modes of oscillation of each sphere and there's a power law behavior for higher periods. The velocity increases for higher diameter spheres at the same driving periods. The highest value of v_{avg} is around 10 mm/s. These are incredibly high velocities for such small swimmers.
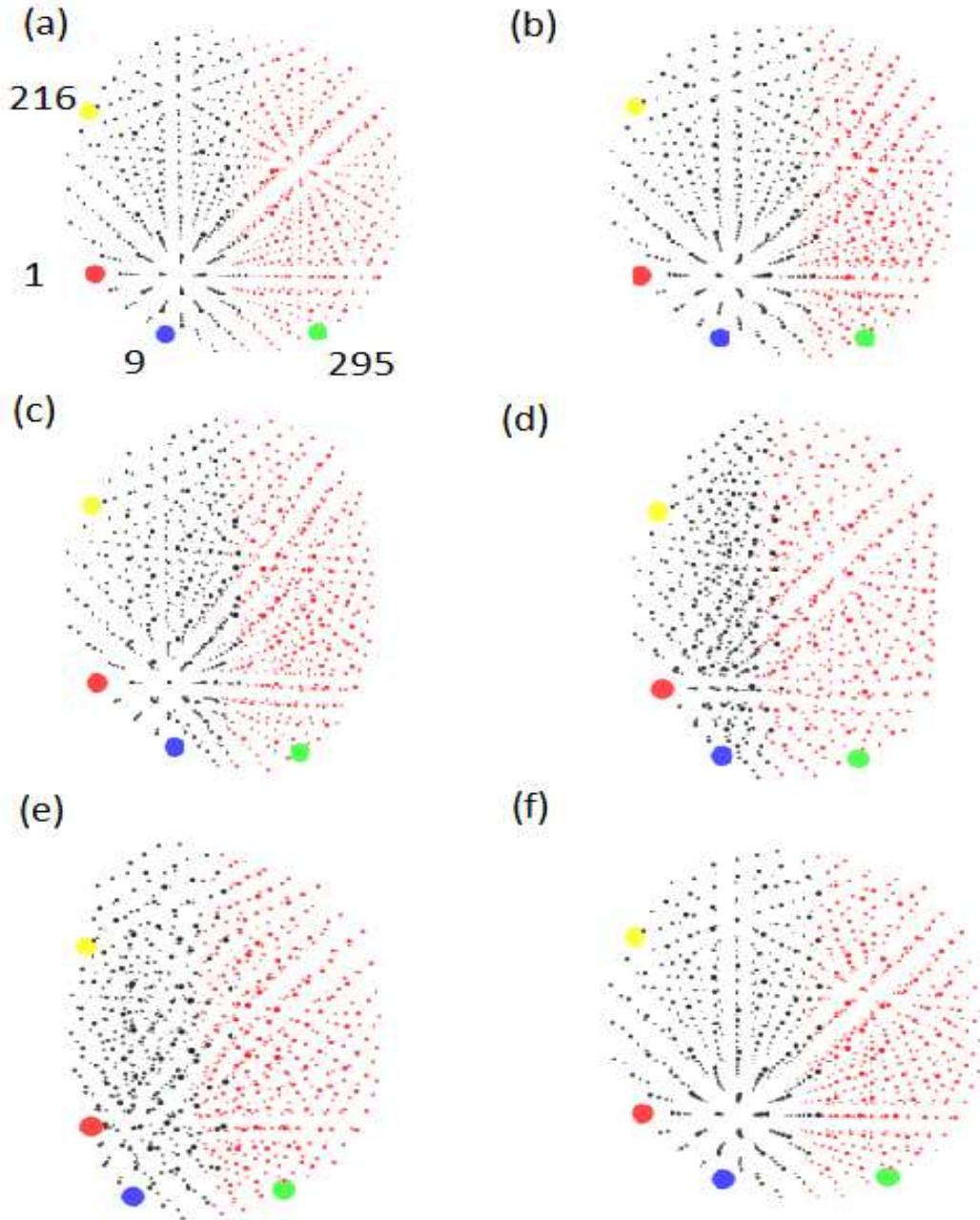
Figure 3.3: Deformation of the sphere over the course of one period of oscillation. The two sides of the sphere are colored differently to indicate the different phase of stimulation in Eq.(3.9) (i.e. one side contracts when the other side expands and vice versa), and four bigger and differently colored particles (marked with IDs - 1,9,216 and 295) on the outer surface which we tracked for further analysis are also indicated. The deformations occur in order from left to right, and the center of mass moves around 1% of the sphere's diameter over the course of an oscillation in this case.
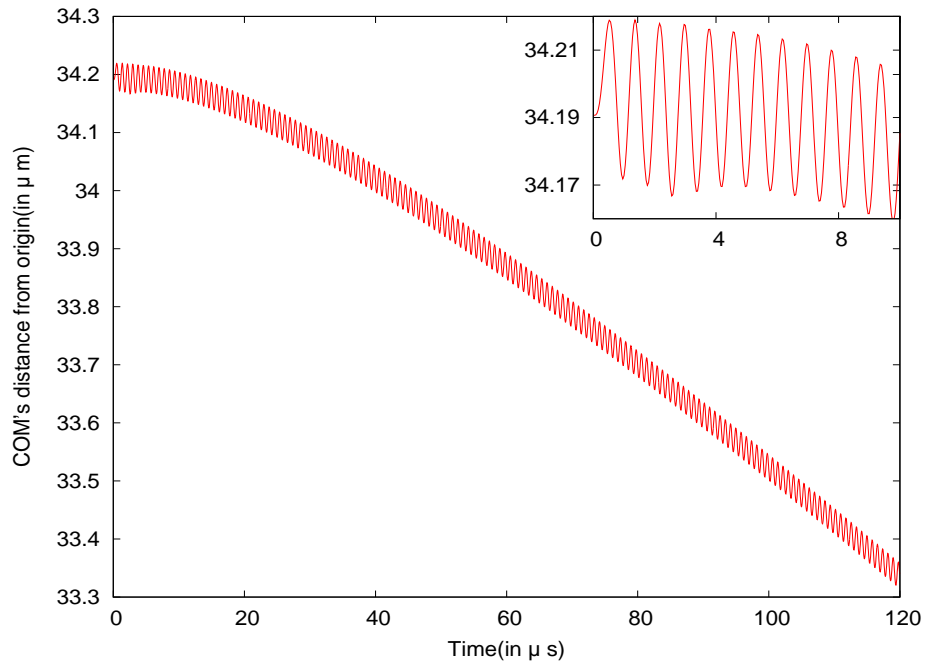
Figure 3.4: Distance of COM (center-of-mass) from origin versus time for a sphere of 10 μm diameter driven at 0.8 μs period. Inset: a zoomed in portion of the same graph.
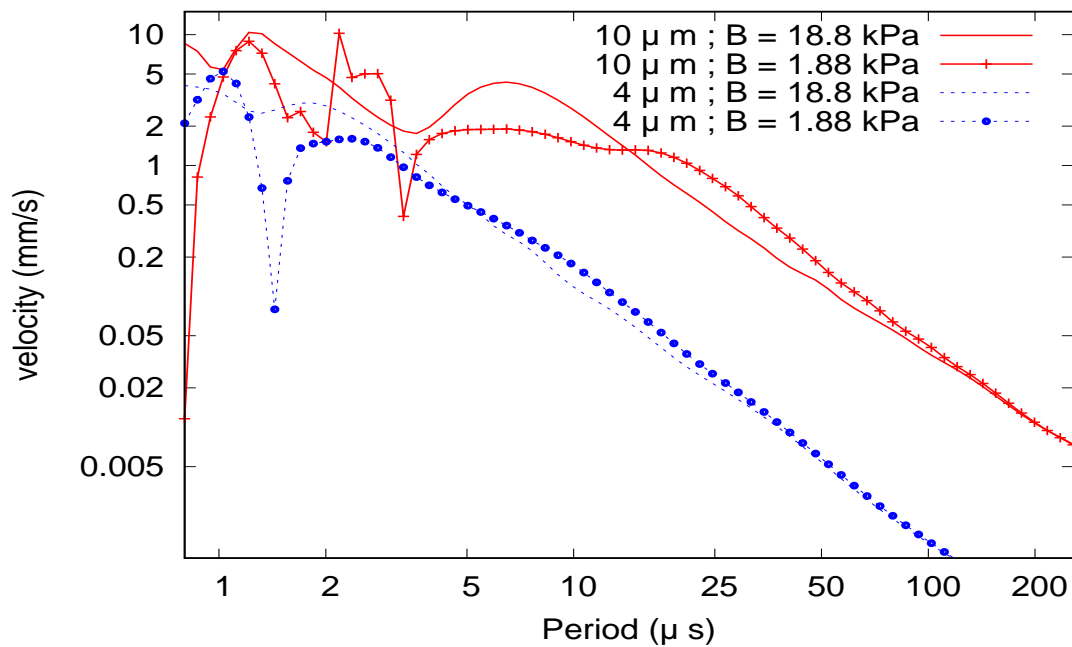
Figure 3.5: Log graph of v_{avg} versus τ for B = 1.88 kPa and B = 18.8 kPa and for spheres with radii 4 μm and 10 μm.

Although the short period/high frequency end of this spectrum is outside of what is observed in biological systems, it is certainly achievable for a swimmer constructed artificially (a nano particle was driven successfully at more than a million rpm (rotations per minute) in [7]). In the low Kilohertz range which could be generated by a biological systems, the higher diameter sphere (10 μm) still achieves velocities of a few μm/s.

The velocity profile produced by these two spheres at various stiffness(B values) can be understood more clearly by having a look at the center-of-mass motion of the spheres. The center-of-mass motion of the spheres (once steady motion is achieved) as a function of time, scaled by the period of the drive, is shown in Fig. 3.6. While there are oscillations about the linear increase of x_{cm} with time, the amount of oscillation varies considerably.
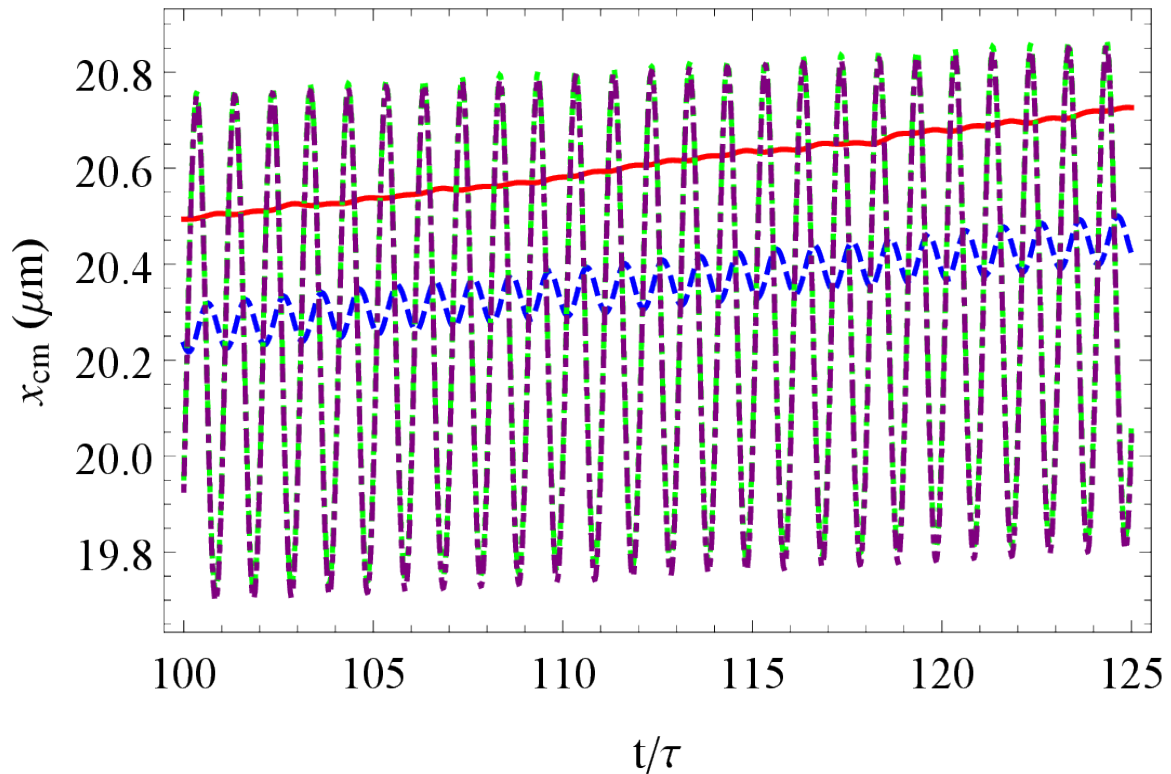
Figure 3.6: Distance of center-of-mass of the sphere from origin versus time scaled by the period of the drive.

At low drive period (high frequency) the motion is fairly efficient in the sense that the forward movement per period is comparable to the overall amplitude (solid red and dashed
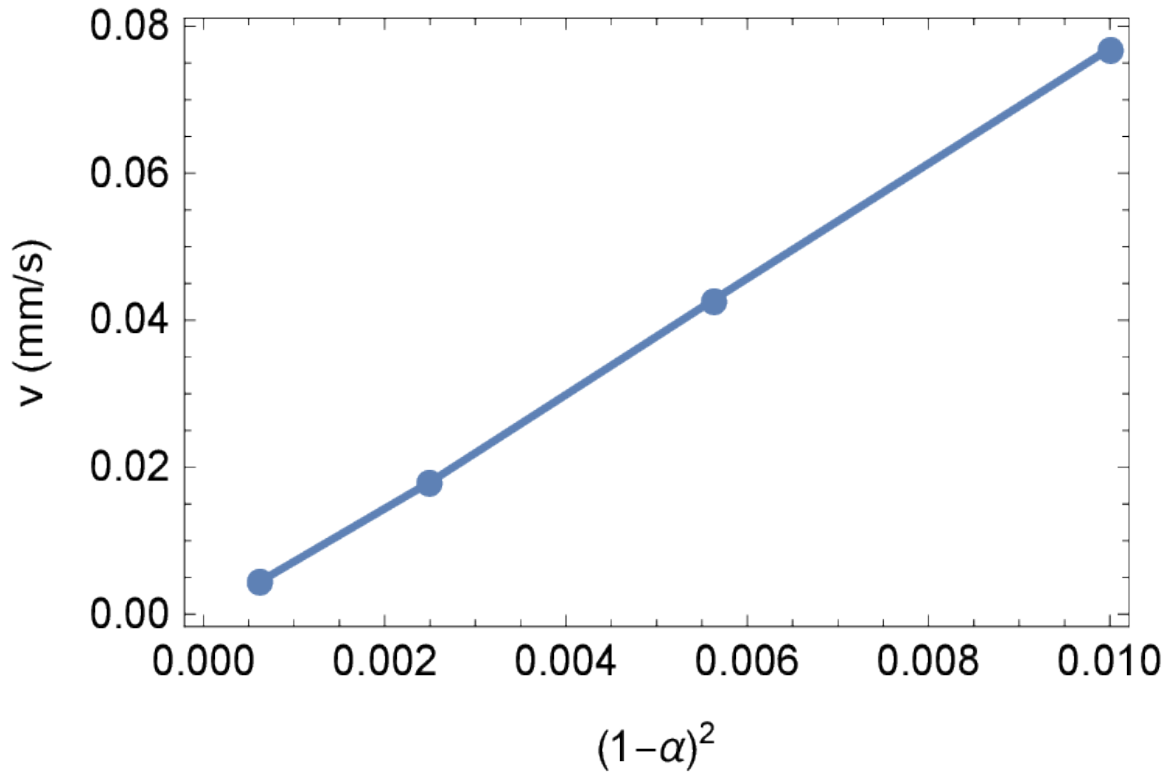
Figure 3.7: Average velocity of a diameter $10\,\mu$m sphere with bulk modulus $B = 1.88$ kPa with drive period $\tau = 64\,\mu$s as a function of the square of the amplitude of the bond oscillations (cf. Eq.(3.9)).

blue lines in Fig. 3.6) whereas at high drive period the sphere advances only a small fraction of its overall amplitude (dotted green and dot-dashed purple lines in Fig. 3.6). Consistent with the observation of the asymptotic velocities (cf. Fig. 3.5), the center-of-mass motion at long periods becomes independent of the elastic constant (the dotted green and dot-dashed purple curve in Fig. 3.6 overlap). However, for short periods the softer (smaller B) sphere has more efficient motion, consistent with its higher velocity in Fig. 3.5.

Additional simulations examined the effect of the driving amplitude on velocity (by varying α in equation (3.9)). As shown in Fig. 3.7, at longer periods ($64\,\mu$s in the figure) the mean velocity is proportional to the amplitude squared, suggesting that the motion is a non-linear response to the drive and therefore beyond the typical Stokes-flow description (linear) based on Eq.(3.6). While the response is well described by the quadratic behavior seen in the Fig.

for most of the range of periods, close to the resonances at shorter period there are considerable deviations, reflecting the nonlinear response and requiring use of the full Navier-Stokes description applied in our analysis rather than the typical linear approximations often used elsewhere for analytic convenience.

Another thing to note is that the lower value of bulk moduli gives rise to larger peaks and resonance effects in the low driving periods, but exhibiting a similar power law behavior at high driving periods as before. This is an important behavior as it is consistent with theoretical predictions as discussed later in the chapter. A fit for the v_{avg} versus τ for the power law region gives a dependence of τ^a with :

$$a = -1.9 \pm 0.1. \tag{3.10}$$

Asymptotically, there appears to be an apparent approach to τ^{-2} for larger periods of oscillation. The asymptotic behavior also appears to be independent of the stiffness of the sphere and only depends on its size (diameter).

3.4 Detailed analysis of results

We performed further analysis on our simulation results and their adherence to our driving model. In particular, we investigated a few aspects to show that the results are consistent with the hypothesized model of propulsion and the forces responsible for the propulsion and their contribution to overall propulsion. We discuss these results in the following sub-sections.

3.4.1 Fluid flow field

We begin our analysis by examining the fluid flow that leads to the motion. Fig. 3.8 shows the flow in orthogonal cross-sections of the system at different points in the period of the motion for one particular case. Near the beginning of the cycle (leftmost panels in Fig. 3.8) the flow field is similar to that of a Stokeslet (force) dipole while later in the cycle it more resembles a source dipole (cf., for example, Fig. 2 in Ref. [27]). The fact that a dipole-like flow field is set
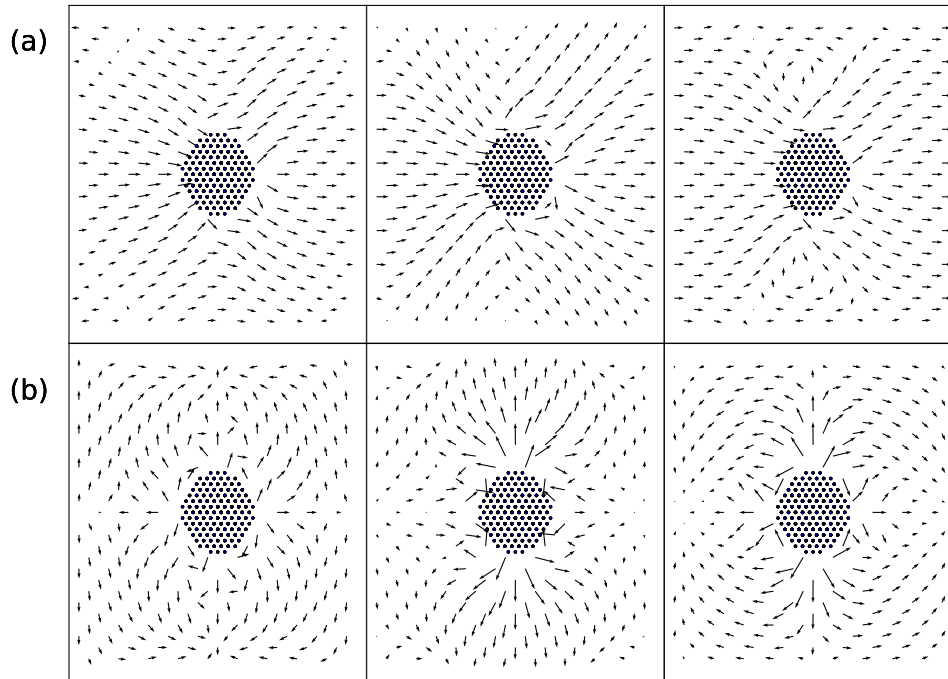
Figure 3.8:   Fluid flow in the (a) plane cutting through the center of the particle where the motion is left to right and (b) plane cutting through the center of the particle where the motion is coming out of the plane towards the viewer. The slices are at different, equally spaced, points during one period of the motion (after a steady mean velocity has been attained). The length of the velocity vectors have a logarithmic scale. The plots shown are for a 10 μm sphere with $B = 1.88$ kPa with a period of 1 μs (same case as the solid red line in Fig. 3.6). The equilibrium cross-section of the sphere is shown only schematically (particles making up the real sphere move in and out of the plane during the motion making the dynamic case hard to represent in 2D).

up is perhaps not too surprising given the fact that we are driving the two halves of our sphere asymmetrically. As such, the appearance of a resulting dipole moment would seem hard to avoid.

3.4.2 Verifying adherence to driving scheme

It is important to show that the periodic driving of the sphere does indeed result in global periodic deformation of the sphere, from its center to the surface. To do this, we selected four constituent particles represented by numeric IDs- 1,9,216 and 295 on the surface of sphere in the plane $z = 0$ as depicted in Fig. 3.9 and previously shown in Fig. 3.3. We tracked their position with respect to the center of mass of sphere over time to see if they oscillate with the same period as the driving period of sphere.

To test whether there was any non-reciprocal motion, we ran simulations of the 10 μm spheres driven at a frequency of 1.25 MHz (0.8 μs period) and 20 kHz (50 μs period), and computed the position of each of these particles with respect to the sphere's center of mass at each timestep. The sphere was driven for 150 periods and first 25 periods were ignored to only track particles once sphere has attained stable motion. The path traced by particles with respect to that of sphere's center of mass is presented in Fig. 3.10. Please note that the Fig. 3.10 only depicts the movement in XY plane as there is almost no movement along the Z axis.

It can be seen in Fig. 3.10, the particles 1,9,216 and 295 all move in a loop with respect to center of mass of sphere, this clearly shows that the movement is periodic and non-reciprocal. The periodic motion of these outer particles reaffirms the adherence of the driven sphere to the driving scheme. It is clear that the deformations are indeed global (i.e they travel from the center to the surface). Notice how the amplitude of deformation is smaller for the sphere driven at higher (50 μs) period, due to the absence of resonance effects that occurs at shorter period(s).

We also plotted the amplitude and investigated the relative phase of the Fourier transform of the particles' (1,9,216 and 295) distance from the sphere's center of mass to reaffirm our findings. We used the data from the simulation of 10 μm diameter sphere driven at 1.25 Mhz frequency. We compared particle 1's amplitude and phase with particle 216's amplitude and

Fig.(a) Position of outer particles

Fig.(b) Top view of z=0 plane
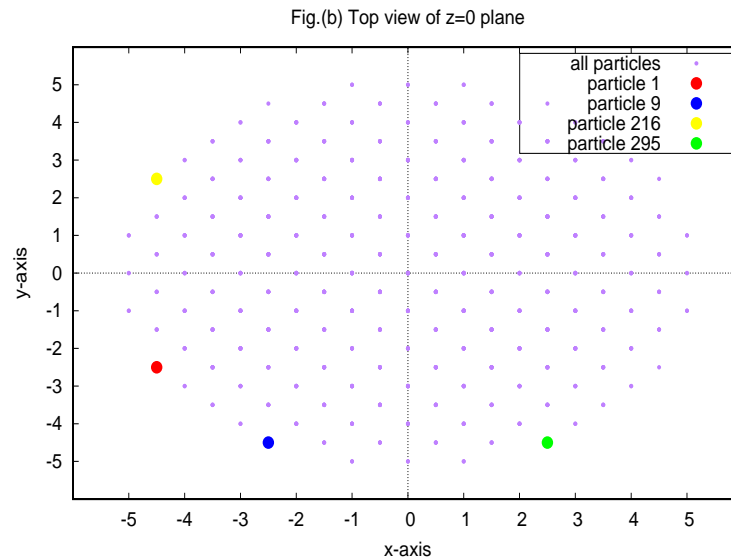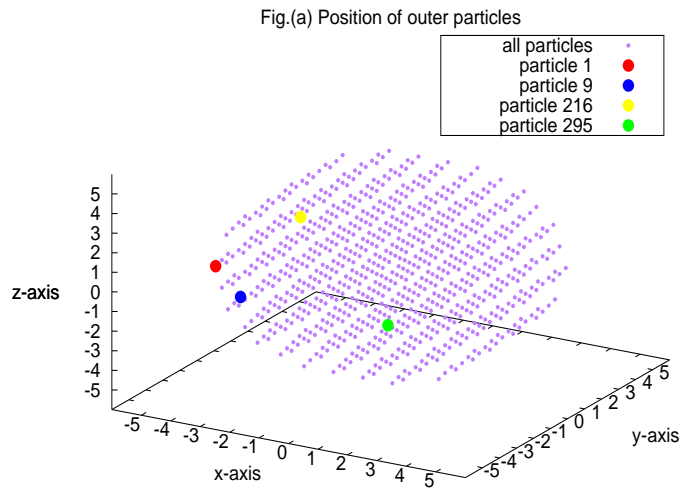
Figure 3.9: Position of outer particles (ID - 1,9,216 and 295) on the sphere presented in Fig(a).
The same four particles are presented again in Fig (b), on the Z=0 plane for a better view.
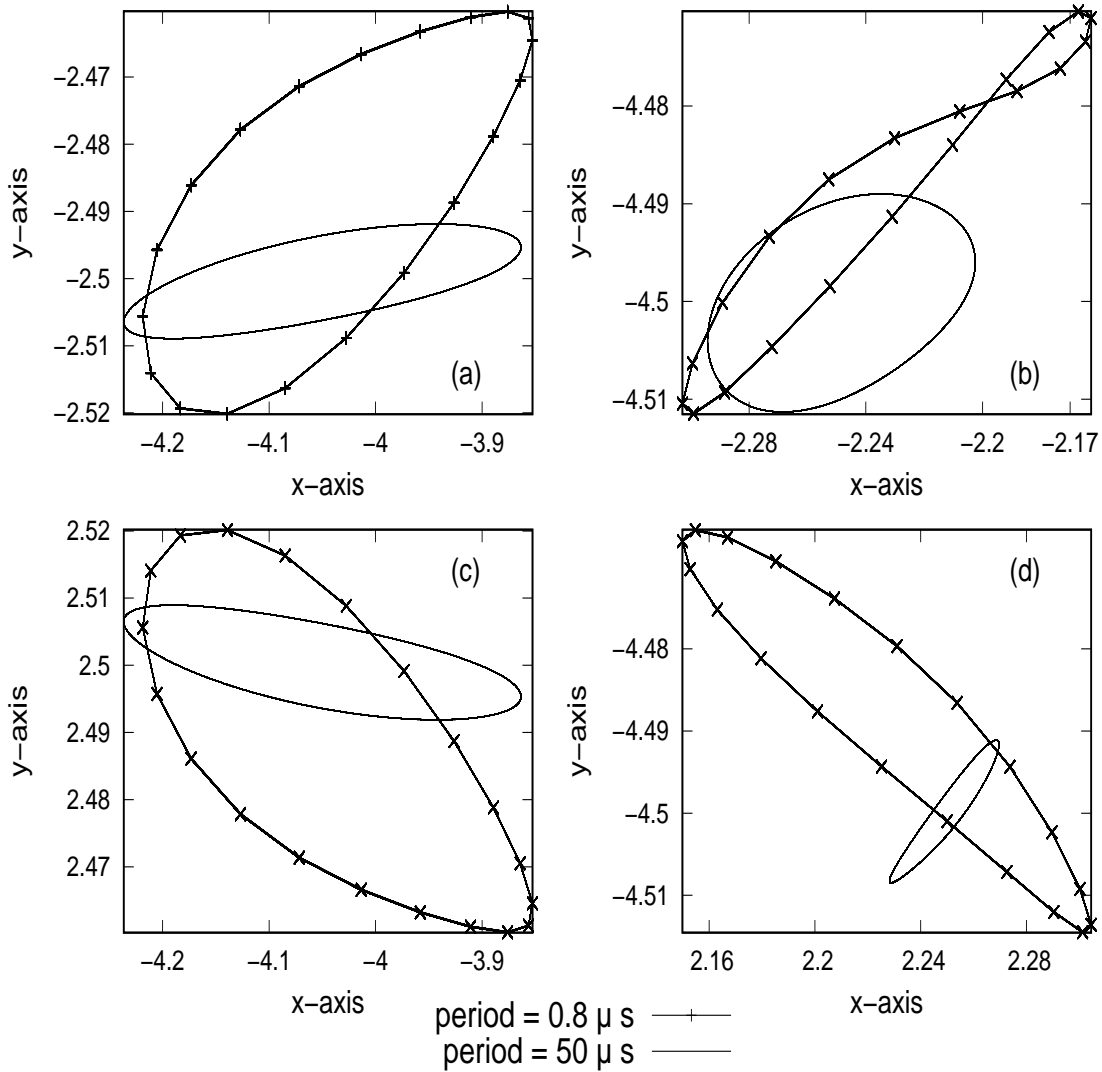
Figure 3.10: Comparison of motion of outer particles (IDs 1,9,216 and 295 as depicted in Fig. 3.3), with respect to center of mass of spheres of diameter 10 μm driven at periods of 0.8 μs and 50 μs. Fig.(a) shows particle 1's track , Fig.(b) shows particle 9's track, Fig.(c) shows particle 216's track and Fig.(d) shows particle 295's track.
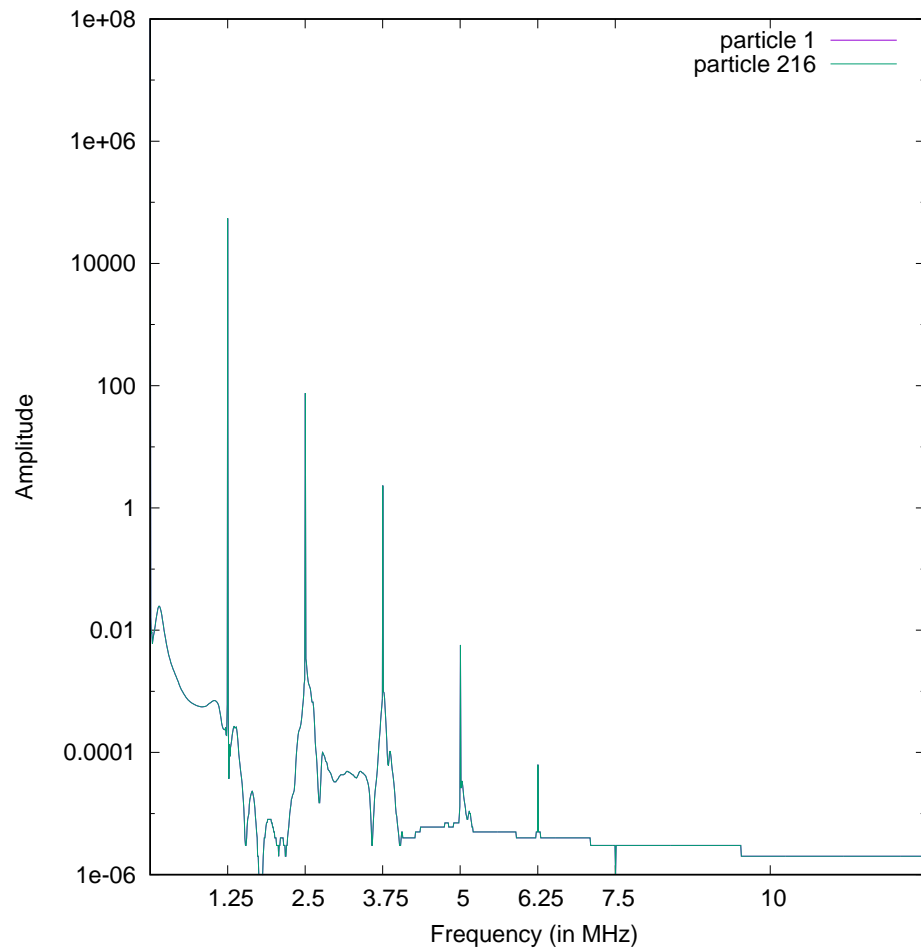
Figure 3.11: Fig. shows the log of absolute value (amplitude) versus frequency plot of the fft of the particles 1 and 216. Note how the transform of both particles 1 and 216 completely overlaps each other. The relative phase for both responses was also investigated at the driving frequency (primary peak in the response at 1.25 MHz) and found to be 0.
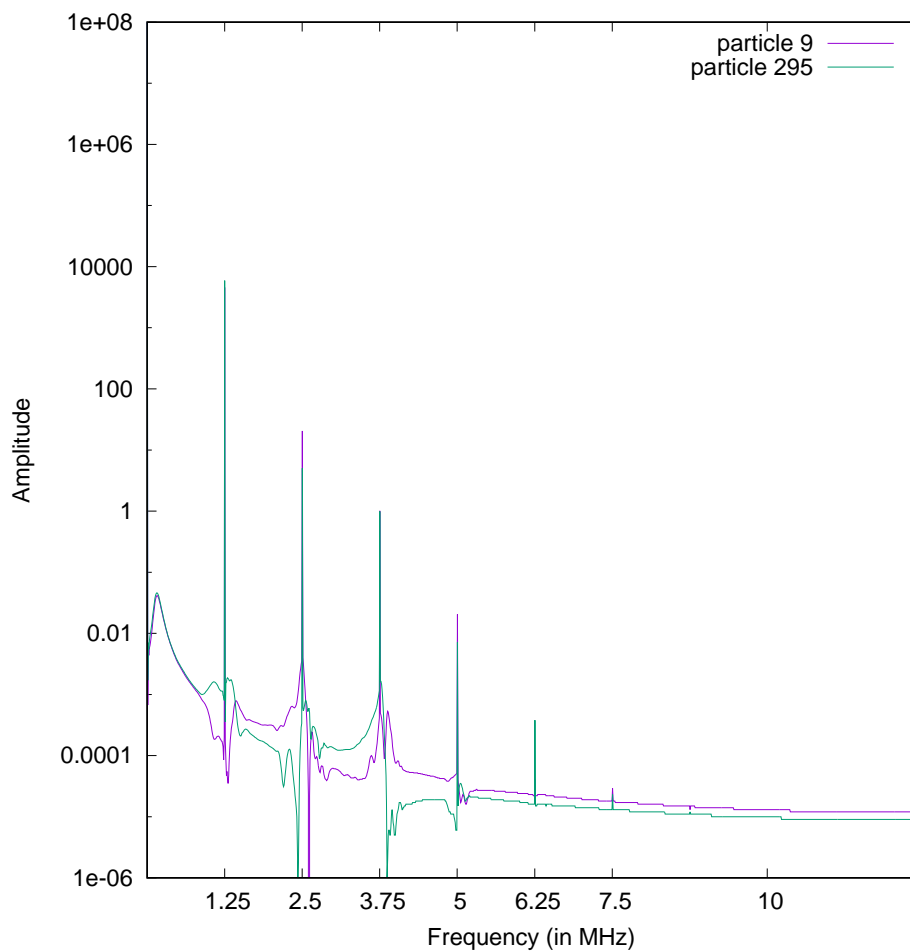
Figure 3.12: Fig. shows the log of absolute value (amplitude) versus frequency plot of the fft of the particles 9 and 295. Note how the transform of both particles 9 and 295 does not overlap suggesting some non-reciprocal motion. The relative phase for both responses were also investigated at the driving frequency (primary peak in the response at 1.25 MHz) and found to be π.

phase, and particle 9's amplitude and phase with particle 295's amplitude and phase. This was done as particles 1 and 216, are both on same side of sphere and hence oscillate *in-phase*, where as particles 9 and 295, are on opposite sides of sphere and hence oscillate π radian *out-of-phase*. In Fig. 3.11 it can be seen that the particles 1 and 216, which are on the same side of the sphere have exactly the same transforms with a peak at 1.25 MHz and the relative phase (at 1.25 MHz) was found to be 0. In Fig. 3.12 it can be seen that the particles 9 and 295 have *non-overlapping* transforms with peak at 1.25 MHz, suggesting that there is some non-reciprocal motion and their relative phase (at 1.25 MHz) was found to be π, confirming that they are indeed π radian out-of-phase as expected.

This analysis confirms that the sphere does move in periodic, but non-reciprocal motion, and that the deformations generated by the driving scheme are global.

3.4.3   Forces behind the propulsion

It is worth investigating to see how much of the driving is due to the inertial forces and how much is due to other forces. We used the data from the simulation of the $10\,\mu$m diameter radius sphere with bulk moduli B = 18.8 kPa. To get the ratio of forces arising from the ∇p term in the Eq. (3.1) to inertial forces, we integrated these forces throughout the *exterior volume*, which is basically the entire volume of the simulation box, minus the volume inside the sphere and a shell extending to four lattice points from the sphere surface. The shell of four lattice points from the surface of the sphere was excluded from the total volume to avoid the presence of moving parts of the sphere in the external volume where forces are integrated.

To get the inertial forces, the absolute value of terms on the left-hand side of the Navier-Stokes equation (3.1) was integrated throughout the exterior volume. For calculating forces arising from the ∇p term in the equation (3.1), the absolute value of ∇p was integrated throughout the exterior volume. For calculating all the derivatives (both time and space), a forward difference was used. The result has been presented in Fig. 3.13 along with the velocity profile of the driven sphere.
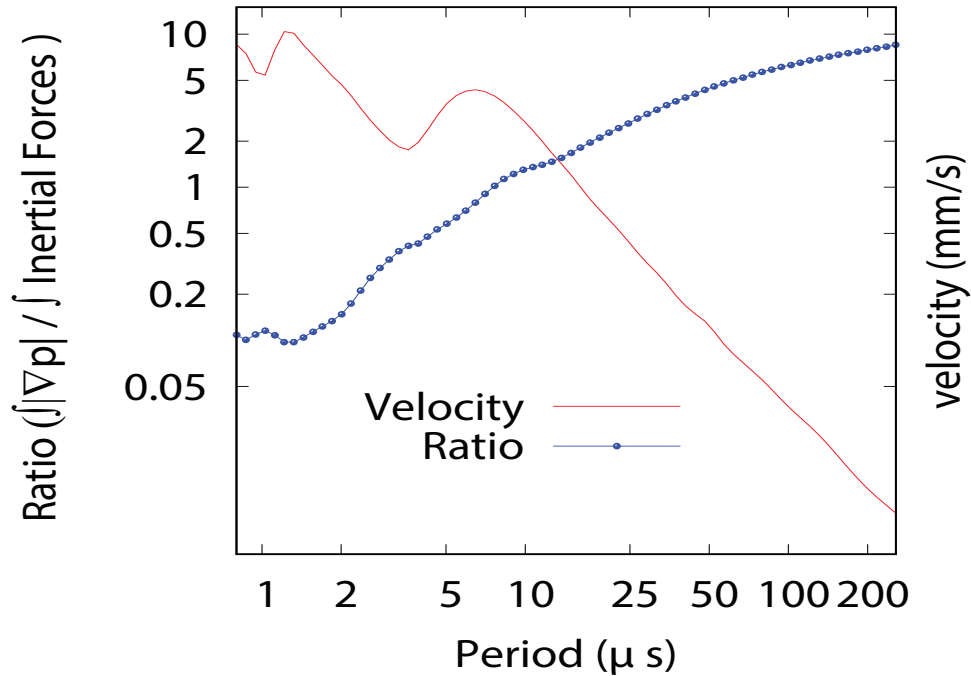
Figure 3.13: Log graph showing the comparison of variation of ratio of $|\nabla p|$ to inertial forces in the system with respect to the driving period of sphere (in μs), and variation of velocity (in mm/s) with respect to driving period (in μs) for a sphere with $10\,\mu$m diameter and bulk moduli $B = 18.8$ kPa.

It can be seen that the inertial forces are dominant when driving velocities are high in low driving period (high frequency) region. However, in the large driving period (low frequency) region the inertial forces are considerably smaller, approaching a tenth of the ∇p forces at longer periods. This leads to the question of whether inertial forces are ever truly negligible. For low periods inertial forces are clearly significant and for longer periods, even though their magnitude is much smaller, the power-law tail of the mean velocity is likely related to the hydrodynamic power-law tail seen in linear response (which we will examine in the next section). As the hydrodynamic tail is intrinsically related to the inertia of the fluid, even at long periods, it would seem that the inertia is important for the mean velocity, even if it is considerably smaller than other terms in Navier-Stokes.

3.4.4 Comparison to theoretical predictions

To further understand the behavior of our model, we compared the behavior of the internal modes of oscillation with continuum mechanical predictions made in recent work by Felderhof [6]. Felderhof shows that for a uniform elastic sphere with shear modulus μ and bulk modulus κ submersed in a fluid, the magnitude of the response observed as the result of an external periodic forcing is highly dependent on its frequency. In particular, he shows the magnitude of the response exhibits several resonant peaks at various frequencies, before exhibiting the behavior of a rigid sphere in the high-frequency limit. While the analysis was for a uniform sphere, rather than the asymmetric sphere we are examining here, it still represents the "mean" bond length behavior of our sphere and so is a reasonable starting point for analysis.

In addition to the linearized Naiver-Stokes equations, Felderhof considers an elastic displacement function $u(r, t)$ of a sphere centered at the origin, which is assumed to satisfy the equation of motion[10].

$$\rho_s \frac{\partial^2 u}{\partial t^2} = \mu \nabla^2 u + \left(\frac{1}{3}\mu + \kappa\right) \nabla \nabla \cdot u + F(t) \ , \tag{3.11}$$

where ρ_s is the sphere density, μ and κ are bulk and shear moduli, and F is a time-dependent external forcing. After Fourier transforming to frequency space, Felderhof derives the relationship

$$U_\omega = \mathcal{Y}_T(\omega) E_\omega \ , \tag{3.12}$$

where U_ω and E_ω are the amplitude of the center-of-mass velocity of the sphere and the applied external forcing in frequency space respectively, and $\mathcal{Y}_T(\omega)$ is a translational admittance function. Felderhof then defines a dimensionless admittance $\hat{F}_T$ of a complex argument $x = a\left(\frac{-i\omega\rho}{\eta}\right)^{1/2}$ given by

$$\hat{F}_T(x) = \frac{4\pi m_p}{3m_f} \eta a \mathcal{Y}_T(\omega) \ , \tag{3.13}$$

where m_p is the mass of the sphere, m_f is the mass of the displaced fluid, and a is the sphere radius. However, to make the admittance more amenable to analysis, Felderhof re-expresses it

in the form

$$\hat{F}_T(x) = \frac{1}{x^2 + MZ_T(x)} \, , \tag{3.14}$$

where $M = \frac{9m_f}{2m_p}$ is related to the mass of the displaced fluid, m_f and the mass of the spherical particle, m_p, and Z_T is a function related to the translational friction coefficient between the force applied and the velocity response.

The behaviour of Z_T is especially key to understanding the elastic behavior of our model. In the general case, Z_T takes the form

$$Z_T(x) = 1 + x + Z_c x^2 + O(x^3) \, , \tag{3.15}$$

which in the case of a no-slip rigid sphere reduces to the case $Z_c = 1/9$ with no higher-order terms. For an elastic sphere, Felderhof shows that

$$Z_c = \frac{1}{9} - \frac{\eta}{a\rho} \frac{c_l + c_t}{c_l c_t} + \frac{\eta^2}{a^2\rho} \frac{403\mu + 210\kappa}{180\mu\kappa} \, , \tag{3.16}$$

where c_l and c_t are velocities related to the elastic constants of the sphere (i.e. μ and κ) with units of velocity. The quantity Z_c itself is dimensionless, but the second and third terms vary inversely with a Reynolds-like number $\mathcal{R} = \frac{\rho ca}{\eta}$ (defined by the inverse of the 2nd term, where c is related to the speed of sound and elastic constants) where the characteristic velocity is now related to c_l and c_t (i.e speeds of sound in the *elastic* media). Since our setup focuses on the small Reynolds number regime, we expect the admittance and friction coefficients to vary dramatically with the fluid and elastic parameters. This explains the high-frequency behavior we have observed in the previous sections.

To further test this prediction, we conducted a series of simulations to measure $\hat{F}_T$ and compare the behavior of our model to the behavior derived in Felderhof's paper. Using a sphere 1 μm in diameter with fixed equilibrium bond lengths r_0 and a bulk modulus of $B = 9.4$ kPa, we applied a series of sinusoidal forcings at various frequencies to our spherical particle, and plotted the motion of its center of mass once the system had reached steady-state behavior. The center of mass velocity curve was was then fitted to a sinusoidal function of the same frequency as the applied forcing, from which the amplitude of response and phase shift (relative to the

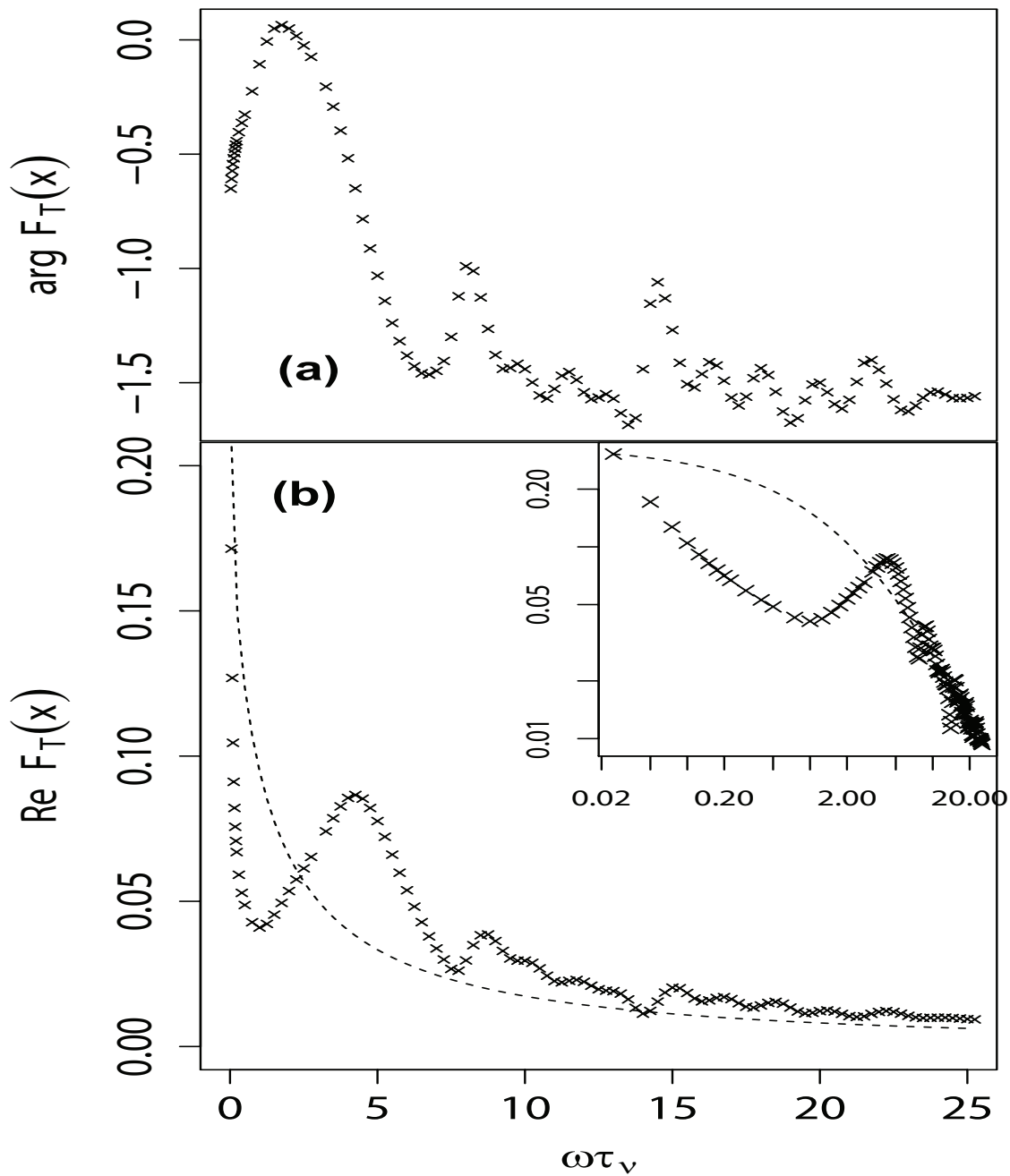Figure 3.14: Measurements of the admittance response function for a uniform elastic sphere. In (a) we plot the argument (F_T is complex) and (b) gives the real part of F_T. The simulation data are indicated by symbols and the dotted line gives the function $\hat{F}_T$ for a no-slip rigid sphere. Both of these are viewed as functions of $\omega\tau_v$. Inset: same data as in (b) but shown using log-log axes.

phase of the forcing) was obtained. Using the relation (3.12) this allowed us to compute $\mathcal{Y}_T$, and consequently $\hat{F}_T$ using (3.13).

In Fig. 3.14 we plot $\hat{F}_T$ for both a theoretical no-slip rigid sphere and the experimentally determined values from our model as functions of the dimensionless frequency $\omega\tau_v$, where $\tau_v = a^2\rho/\eta$ is the viscous relaxation time. Viewing Fig. 3.14, it is clear our model exhibits resonant behavior at low values of $\omega\tau_v$ similar to those predicted by Felderhof's results [6], before approaching the rigid no-slip approximation in the high-($\omega\tau_v$) limit. The non-monotonic behavior of the admittance for the elastic sphere allows the sphere to store internal elastic behavior and release it later in the cycle and can be extremely important for the motion. Unfortunately, such analysis is only applicable for its qualitative behavior, as accurately modeling an hcp lattice requires more than two independent elastic constants. Analytically modeling the split sphere would be even more difficult.

However, despite these limitations there are clear implications from this analysis. As seen above, at high frequencies there are many resonant peaks that depend on both details of the sphere, such as its elastic constants, as well as details of the fluid, such as viscosity. However the long-time behavior of the spheres velocity is found to be [6]

$$\mathbf{U}(t) \approx \frac{1}{12\rho(\pi\mu t/\rho)^{3/2}}\mathbf{E} \tag{3.17}$$

where $\mathbf{E}$ is the drive amplitude, a result that is independent of the elastic properties of the sphere. This response is similar to what is seen in the mean velocity of the sphere in Fig. 3.5: resonant peaks at short periods (high frequency) that depend on the elastic constants of the sphere and a power-law behavior for long drive periods that is independent of the elastic constants.

The presence of power-law tails also supplies a reason why a simple comparison of the terms in Navier-Stokes Eq.(3.1), as done in Eq.(3.3), can be problematic as it is not appropriate to use the period T as a time scale when the long-time response is a power-law (i.e. scale-free: effectively the system does not forget what went on before). Further, as we saw in the last section, the flow field resembles that of a Stokeslet (force) dipole, which decays as $1/R^2$, or a source dipole, which decays as $1/R^3$. As a result, using the particle radius as the length scale

in Eq.(3.3), when this length scale does not dictate the longest length scale in the flow field is also questionable.

3.5 Conclusion

Through computer simulation of an elastic spherical particle in a lattice-Boltzmann fluid, we have shown that it is possible to use internal elastic modes of oscillation to overcome limitations imposed by the Scallop theorem. In particular, we found that by varying the bond lengths of a spherical particle sinusoidally, we were able to produce propulsion through reciprocal drive even with driving frequencies in the low kilohertz range. In our case, even though the drive is reciprocal, the elastic modes excited in the sphere result in periodic but non-reciprocal motion of the sphere's surface, driving dipole-like flow fields in the fluid. At high frequencies, the speeds obtained by are model are very high, in the mm/s range, and even at low frequencies the particles can move several body lengths per second. High frequency driving (more than a million rpm) of nano particles has recently been demonstrated in light-driven submersible nano machines [7] and the speeds obtained by our model are comparable for a much wider range of particle sizes. In particular, current technology should be capable of creating micro particles with the properties of our model which could be used to replicate this behavior by stimulation using an external electric field.

Chapter 4

Conclusions

In the thesis presented above, in Chapter 1 we discussed the role of the Scallop theorem and the limitations it puts on swimmers in a microscopic domain. We explained the theorem in detail, along with the scenarios where it does not apply (such as non-reciprocal motion using multiple degrees of freedom). The emphasis was on the fact that to the best of our knowledge, no one has demonstrated that inertia could play a significant role in propulsion of a neutrally buoyant swimmer in a Newtonian fluid. We mentioned the methodologies that go into such a MD simulation and briefly discussed the simulation tool used for our simulations.

In Chapter 2, we began exploring the methodologies used for such simulations. We focused primarily on the numerical integration techniques used. In LAMMPS, the integrator used to solve Newton's equations of motion is the velocity-Verlet scheme. We started by explaining why velocity-Verlet makes for an excellent choice in MD simulations. We then emphasized the fact that the implementation of the velocity-Verlet mostly used in MD simulations is a non-adaptive single timestep scheme. We demonstrated that for an MD simulation where particles interact via a non-bonded pairwise Lennard-Jones potential, using a non-adaptive single timestep scheme is not the most effective method. We presented an adaptive single timestep version of the velocity-Verlet scheme and showed that although it is better than the non-adaptive version, it still does not give significant performance benefits at large densities/large simulation box sizes.

In Chapter 2, we also presented a derivation of an expression that gives us the stability criteria for the timestep in such a simulation. We used this criteria as passive control - we tracked it and demonstrated that it could be an effective control and could be used to check if the current adaptive timestep results in an unstable simulation. Other than stability, we had four active controls, giving us the range for truncation errors and adaptive timesteps.

We concluded the chapter with a discussion of ongoing work on the multiple timestep version of the velocity-Verlet scheme. We discussed how the scheme works in principle. We also mentioned the group of multiple timestep algorithms - RESPA that our scheme is based up on. It was shown that timesteps within a simulation with a separation of timescales can be assigned depending on the potentials (in case of multiple potentials acting on the system) or by the timescales associated with a single potential.

In Chapter 3, we presented the elastic spherical swimmer we used for our numerical experiment. We explained the hcp structure of the swimmer consisting 856 individual particles with one outer layer to interact with Lattice Boltzmann fluid the swimmer was submerged in. We used a hybrid MD-LBM simulation package implemented in LAMMPS. We discussed the driving scheme of the swimmer, using contraction and expansion of harmonic bonds between constituent particles given by equation (3.9). The expansions and contractions in two hemispheres of the sphere were out of phase resulting in a motion resembling an off-balance washing machine "walking" across the floor.

We performed several simulation runs with spheres of radii - $4\mu m$ and $10\mu m$, and bulk moduli B=1.88 KPa and B=18.8 KPa. We analyzed the relation between the driving period of the elastic spheres and the velocities attained by them and presented the result in Fig. 3.5. It was observed that the sphere attained high velocities (order of a few mm/sec) which is quite high for such a microscopic swimmer. Even in the higher period (low frequency) range, velocities of order of a few μm/s were observed.

We also tracked four particles on the surface of the sphere to show that their motion follows the driving scheme and the deformations caused due to the driving scheme reach the surface of the sphere. We presented the results in Fig. 3.10 where it can be seen that the outer particles do

follow the driving scheme and deformations in the sphere are indeed global. We also plotted the Fourier transform (amplitude and frequency) of the outer particles' distance from the sphere's COM (center of mass) and showed that the driving frequency was exactly that at which the sphere was driven and also that the phase difference between two particles on the same side of the sphere was 0, and on the opposite sides was π, in agreement with the driving scheme.

We tested the sphere with variable amplitudes of driving and found that the average velocity attained was proportional to the amplitude squared as shown in Fig. 3.7. We then analyzed the simulation results to see what were the forces behind the sphere's motion. We were interested to determine what part of the driving is due to inertial forces and what part is due to ∇p forces. We integrated the left-hand side of Navier-Stoke's equation (3.1), throughout the *exterior volume* which is the volume of the simulation box minus the volume of the sphere and a shell of four lattice points from the sphere's surface, to get the inertial forces. We integrated right-hand side of Navier-Stoke's equation throughout the exterior volume to get the elastic forces. We plotted the ratio of elastic to inertial forces in Fig. 3.13. It was found that inertia actually plays a significant role's in sphere's driving. Even at large driving periods (low frequencies) where the sphere velocities were low, inertia still was responsible for about 1/10th of the driving forces.

We concluded Chapter 3 by presenting the theoretical predictions for an elastic uniform sphere by Felderhof [6], and comparing them to the results we observed. Although the analysis by Felderhof is on a uniform elastic sphere under external periodic forcing, it is still useful to compare it to our experiment, as it represents the mean bond length behavior of our sphere. We found that the resonant peaks observed in the velocity versus sphere diameter graph shown in Fig. 3.5, is similar to the behavior of an uniform elastic sphere driven under external force as shown in Fig. 3.14. It should be noted though, that such a comparison is purely qualitative and not accurate as theoretically modeling a sphere with hcp lattice and two split hemispheres is a difficult task. Nevertheless, it was shown that the behavior of our sphere is indeed in agreement with theoretical prediction for a similar driven sphere.

Finally, to conclude the thesis it is worthwhile to talk about some applications such an elastic spherical swimmer might have. Since, we proved that the driving frequencies are in reach

of some piezoelectric materials under external electric fields [12], it is completely possible to create such a swimmer and drive them. Such a swimmer which can store inertia and advance itself, can be very useful in cargo-carrying (for example drug delivery in a blood stream etc.). Another potential application is using swaths of such swimmers made with catalytic material fused in them and floating back-and-forth held under external electric field, as a catalyst for a reaction (such as catalytic converters used in cars). This would vastly increase the surface area offered by such catalysts, as the entire surface of swimmers are available for catalysis of the reactions.

Bibliography

[1] Daniel Ahmed, Thierry Baasch, Bumjin Jang, Salvador Pane, Jurg Dual, and Bradley J Nelson. Artificial swimmers propelled by acoustically activated flagella. *Nano Letters*, 16(8):4968–4974, 2016.

[2] NW Ashcroft and ND Mermin. Solid State Physics. 1976.

[3] Antoine Barbot, Dominique Decanini, and Gilgueng Hwang. On-chip microfluidic multimodal swimmer toward 3D navigation. *Scientific Reports*, 6, 2016.

[4] Amy M Collinsworth, Sarah Zhang, William E Kraus, and George A Truskey. Apparent elastic modulus and hysteresis of skeletal muscle cells throughout differentiation. *American Journal of Physiology-Cell Physiology*, 283(4):C1219–C1227, 2002.

[5] Erwin Fehlberg. CLASSICAL FIFTH-, SIXTH-, SEVENTH-, AND EIGHTH-ORDER RUNGE-KUTTA FORMULAS WITH STEPSIZE. *NASA Technical Report*, 1968.

[6] B. U. Felderhof. Jittery velocity relaxation of an elastic sphere immersed in a viscous incompressible fluid. *Physical Review*, 89, 2014.

[7] Víctor García-Lopez, Pinn-Tsong Chiang, Fang Chen, Gedeng Ruan, Angel A Martí, Anatoly B Kolomeisky, Gufeng Wang, and James M Tour. Unimolecular Submersible Nanomachines. Synthesis, Actuation, and Monitoring. *Nano Letters*, 15(12):8229–8239, 2015.

[8] Darryl D Humphreys, Richard A Friesner, Bruce J Berne, et al. A multiple-time-step molecular dynamics algorithm for macromolecules. *Journal of Physical Chemistry*, 98(27):6885–6892, 1994.

[9] Vasily Kantsler, Jörn Dunkel, Martyn Blayney, and Raymond E Goldstein. Rheotaxis facilitates upstream navigation of mammalian sperm cells. *Elife*, 3:e02403, 2014.

[10] L. D. Landau and E.M. Lifshitz. *Theory of Elasticity*. 1959.

[11] Sandia Labs. LAMMPS. `http://lammps.sandia.gov/doc/Manual.html`. [Online; accessed=2017-03-14].

[12] LD Landau and EM Lifshitz. Electrodynamics of Continuous Media. *Pergamon Press Oxford*.

[13] M Loferer-Krößbacher, J Klima, and R Psenner. Determination of bacterial cell dry mass by transmission electron microscopy and densitometric image analysis. *Applied and Environmental Microbiology*, 64(2):688–694, 1998.

[14] FE Mackay and Colin Denniston. Coupling MD particles to a lattice-Boltzmann fluid through the use of conservative forces. *Journal of Computational Physics*, 237:289–298, 2013.

[15] FE Mackay, Santtu TT Ollila, and Colin Denniston. Hydrodynamic forces implemented into LAMMPS through a lattice-Boltzmann fluid. *Computer Physics Communications*, 184(8):2021–2031, 2013.

[16] Sebastien Michelin and Eric Lauga. Geometric tuning of self-propulsion for Janus catalytic particles. *arXiv Preprint arXiv:1701.02569*, 2017.

[17] Bradley J Nelson, Ioannis K Kaliakatsos, and Jake J Abbott. Microrobots for minimally invasive medicine. *Annual Review of Biomedical Engineering*, 12:55–85, 2010.

[18] Santtu TT Ollila, Christopher J Smith, Tapio Ala-Nissila, and Colin Denniston. The Hydrodynamic Radius of Particles in the Hybrid Lattice-Boltzmann Molecular Dynamics Method. *Multiscale Modeling & Simulation*, 11(1):213–243, 2013.

[19] Jae-Sung Park, Suk-Heung Song, and Hyo-Il Jung. Continuous focusing of microparticles using inertial lift force and vorticity via multi-orifice microfluidic channels. *Lab on a Chip*, 9(7):939–948, 2009.

[20] Christian Peters, Silvan Staufert, and Christofer Hierold. Strain engineered 3D magnetic micro actuators with programmed magnetic anisotropy. In *Micro Electro Mechanical Systems (MEMS), 2017 IEEE 30th International Conference on*, pages 258–261. IEEE, 2017.

[21] Steve Plimpton. Fast parallel algorithms for short-range molecular dynamics. *Journal of Computational Physics*, 117(1):1–19, 1995.

[22] Edward M Purcell. Life at low Reynolds number. *American Journal of Physics*, 45(1):3–11, 1977.

[23] Tian Qiu, Tung-Chun Lee, Andrew G Mark, Konstantin I Morozov, Raphael Münster, Otto Mierka, Stefan Turek, Alexander M Leshansky, and Peer Fischer. Swimming by reciprocal motion at low Reynolds number. *Nature Communications*, 5, 2014.

[24] G. Segre and A. Silberberg. Behaviour of macroscopic rigid spheres in Poiseuille flow Part 1. Determination of local concentration by statistical analysis of particle passages through crossed light beams. *Journal of Fluid Mechanics*, 14(1):115–135, 1962.

[25] G. Segre and A. Silberberg. Behaviour of macroscopic rigid spheres in Poiseuille flow Part 2. Experimental results and interpretation. *Journal of Fluid Mechanics*, 14(01):136–157, 1962.

[26] R. Simha. Untersuchungen über die viskosität von suspensionen und lösungen. *Kolloid-Zeitschrift*, 76(1):16–19, 1936.

[27] Saverio E. Spagnolie and Eric Lauga. Hydrodynamics of self-propulsion near a boundary: predictions and accuracy of far-field approximations. *Journal of Fluid Mechanics*, 700:105147, 2012.

[28] Geoffrey Ingram Taylor. *Low Reynolds number flows*. Released by Encyclopaedia Britannica Educational Corporation, 1985.

[29] David J Tritton. *Physical Fluid Dynamics*. Springer Science & Business Media, 2012.

[30] Mark E Tuckerman and Michele Parrinello. Integrating the Car–Parrinello equations. II. Multiple time scale techniques. *The Journal of Chemical Physics*, 101(2):1316–1329, 1994.

[31] MBBJM Tuckerman, Bruce J Berne, and Glenn J Martyna. Reversible multiple time scale molecular dynamics. *The Journal of Chemical Physics*, 97(3):1990–2001, 1992.

[32] Franziska Ullrich, Christos Bergeles, Juho Pokki, Olgac Ergeneman, Sandro Erni, George Chatzipirpiridis, Salvador Pané, Carsten Framme, and Bradley J Nelson. Mobility experiments with microrobots for minimally invasive intraocular Surgery Microrobot experiments for intraocular surgery. *Investigative Ophthalmology & Visual Science*, 54(4):2853–2863, 2013.

[33] Loup Verlet. Computer "experiments" on classical fluids. I. Thermodynamical properties of Lennard-Jones molecules. *Physical Review*, 159(1):98, 1967.

[34] John A White. Lennard-Jones as a model for argon and test of extended renormalization group calculations. *The Journal of Chemical Physics*, 111(20):9352–9356, 1999.

[35] Wen-Chun Yeh, Pai-Chi Li, Yung-Ming Jeng, Hey-Chi Hsu, Po-Ling Kuo, Meng-Lin Li, Pei-Ming Yang, and Po Huang Lee. Elastic modulus measurements of human liver and correlation with pathology. *Ultrasound in Medicine & Biology*, 28(4):467–474, 2002.

[36] Hailing Yu, Andrii Kopach, Vyacheslav R Misko, Anna A Vasylenko, Denys Makarov, Fabio Marchesoni, Franco Nori, Larysa Baraban, and Gianaurelio Cuniberti. Microswim-

mers: Confined Catalytic Janus Swimmers in a Crowded Channel: Geometry-Driven Rectification Transients and Directional Locking (Small 42/2016). *Small*, 12(42):5912–5912, 2016.

[37] Tony S Yu, Eric Lauga, and AE Hosoi. Experimental investigations of elastic tail propulsion at low Reynolds number. *Physics of Fluids*, 18(9):091701, 2006.

Appendix A

Copyright Permissions

Permission for figure 1.1

Curriculum Vitae

Name: Shikhar Dwivedi

Post-Secondary   B.Tech. Information Technology

Education and   Harcourt Butler Technolgical Institute

Degrees: Kanpur, India

2009 - 2013

M.Sc. Applied Mathematics

University of Western Ontario

London, ON

2015 - current

Related Work   Graduate Teaching Assistant

Experience: The University of Western Ontario

2015 - 2017

Honors and   Western Graduate Research Scholarship, 2015-2017

Awards: Western Teaching and Research Assistantship, 2015-2017